JOURNAL OF GEOPHYSICAL RESEARCH, VOL. 106, NO. D22, PAGES 28,371–28,398, NOVEMBER 27, 2001

Indian Ocean Experiment: An integrated analysis of the climate forcing and effects of the great Indo-Asian haze

V. Ramanathan,[1] P. J. Crutzen,[1,2] J. Lelieveld,[2] A. P. Mitra,[3] D. Althausen,[4] J. Anderson,[5] M. O. Andreae,[2] W. Cantrell,[6] G. R. Cass,[7] C. E. Chung,[1] A. D. Clarke,[8] J. A. Coakley,[9] W. D. Collins,[10] W. C. Conant,[1] F. Dulac,[11] J. Heintzenberg,[4] A. J. Heymsfield,[10] B. Holben,[12] S. Howell,[8] J. Hudson,[13] A. Jayaraman,[14] J. T. Kiehl,[10] T. N. Krishnamurti,[15] D. Lubin,[1] G. McFarquhar,[10] T. Novakov,[16] J. A. Ogren,[17] I. A. Podgorny,[1] K. Prather,[18] K. Priestley,[19] J. M. Prospero,[20] P. K. Quinn,[21] K. Rajeev,[22] P. Rasch,[10] S. Rupert,[1] R. Sadourny,[23] S. K. Satheesh,[1] G. E. Shaw,[24] P. Sheridan,[17] and F. P. J. Valero[1]

Abstract. Every year, from December to April, anthropogenic haze spreads over most of the North Indian Ocean, and South and Southeast Asia. The Indian Ocean Experiment (INDOEX) documented this Indo-Asian haze at scales ranging from individual particles to its contribution to the regional climate forcing. This study integrates the multiplatform observations (satellites, aircraft, ships, surface stations, and balloons) with one- and four-dimensional models to derive the regional aerosol forcing resulting from the direct, the semidirect and the two indirect effects. The haze particles consisted of several inorganic and carbonaceous species, including absorbing black carbon clusters, fly ash, and mineral dust. The most striking result was the large loading of aerosols over most of the South Asian region and the North Indian Ocean. The January to March 1999 visible optical depths were about 0.5 over most of the continent and reached values as large as 0.2 over the equatorial Indian ocean due to long-range transport. The aerosol layer extended as high as 3 km. Black carbon contributed about 14% to the fine particle mass and 11% to the visible optical depth. The single-scattering albedo estimated by several independent methods was consistently around 0.9 both inland and over the open ocean. Anthropogenic sources contributed as much as 80% (±10%) to the aerosol loading and the optical depth. The in situ data, which clearly support the existence of the first indirect effect (increased aerosol concentration producing more cloud drops with smaller effective radii), are used to develop a composite indirect effect scheme. The Indo-Asian aerosols impact the radiative forcing through a complex set of heating (positive forcing) and cooling (negative forcing) processes. Clouds and black carbon emerge as the major players. The dominant factor, however, is the large negative forcing (-20 ± 4 W m^{-2}) at the surface and the comparably large atmospheric heating. Regionally, the absorbing haze decreased the surface solar radiation by an amount comparable to 50% of the total ocean heat flux and nearly doubled the lower tropospheric solar heating. We demonstrate with a general circulation model how this additional heating significantly perturbs the tropical rainfall patterns and the hydrological cycle with implications to global climate.

[1]Center for Atmospheric Sciences, Scripps Institution of Oceanography, University of California, San Diego, California.
[2]Max Planck Institute for Chemistry, Mainz, Germany.
[3]National Physical Laboratory, New Delhi, India.
[4]Institute for Tropospheric Research, Leipzig, Germany.
[5]Department of Geology and Chemistry, Arizona State University, Tempe, Arizona.
[6]Department of Chemistry, Indiana University, Bloomington, Indiana.
[7]School of Civil and Environmental Engineering, Georgia Institute of Technology, Atlanta, Georgia.
[8]Department of Oceanography, University of Hawaii, Honolulu, Hawaii.
[9]College of Oceanic and Atmospheric Sciences, Oregon State University, Corvallis, Oregon.
[10]National Center for Atmospheric Research, Boulder, Colorado.
[11]Laboratoire des Sciences du Climat et de l'Environment, Gif sur Yvette, France.

Paper number 2001JD900133.
0148-0227/01/2001JD900133$09.00

[12]NASA Goddard Space Flight Center, Greenbelt, Maryland.
[13]Desert Research Institute, Reno, Nevada.
[14]Physical Research Laboratory, Ahmedabad, India.
[15]Department of Meteorology, Florida State University, Tallahassee, Florida.
[16]Lawrence Berkeley National Laboratory, Berkeley, California.
[17]Climate Monitoring and Diagnostics Laboratory, NOAA, Boulder, Colorado.
[18]Department of Chemistry, University of California, Riverside, California.
[19]NASA Langley Research Center, Hampton, Virginia.
[20]Rosenstiel School of Marine and Atmospheric Science, University of Miami, Miami, Florida.
[21]Pacific Marine Environmental Laboratory, NOAA, Seattle, Washington.
[22]Space Physics Laboratory, VSSC, Thiruvananthapuram, Kerala State, India.
[23]Laboratoire de Meteorologie Dynamique, Paris, France.
[24]Geophysical Institute, University of Alaska Fairbanks, Fairbanks, Alaska.

1. Introduction

It is now well documented [e.g., *Langner and Rodhe*, 1991; *Intergovernmental Panel on Climate Change (IPCC)*, 1995; *Schwartz*, 1996] that anthropogenic activities have increased atmospheric aerosol concentrations. Both fossil fuel combustion and biomass burning [*Andreae and Crutzen*, 1997] contribute to aerosol production, by emitting primary aerosol particles (e.g., fly ash, dust, and black carbon) and aerosol precursor gases (e.g., SO_2, NO_x, and volatile organic compounds) which form secondary aerosol particles through gas-to-particle conversion. Secondary aerosols also have biogenic sources (dimethyl sulfide from marine biota and nonmethane hydrocarbons from terrestrial vegetation). The secondary particles formed are categorized as inorganic (e.g., sulfates, nitrates, ammonia) or organic (e.g., condensed volatile organics). The combination of organics and black carbon aerosols are also referred to as carbonaceous aerosols. Aerosols exist in the atmosphere in a variety of hybrid structures: externally mixed, internally mixed, coated particles or most likely a combination of all of the above. Our primary interest in this paper is on the climate forcing of aerosols, which is defined first. A change in radiative fluxes (be it at the surface or the top-of-the atmosphere) due to aerosols is referred to as aerosol radiative forcing and that due to anthropogenic aerosols is referred to as anthropogenic aerosol forcing; and the difference between the two forcing terms is due to natural aerosols. Anthropogenic aerosols can modify the climate forcing directly by altering the radiative heating of the planet [*Coakley and Cess*, 1985; *Charlson et al.*, 1991], indirectly by altering cloud properties [*Twomey*, 1977; *Albrecht*, 1989; *Rosenfeld*, 2000], and semidirectly by evaporating the clouds [*Hansen et al.*, 1997; *Kiehl et al.*, 1999; *Ackerman et al.*, 2000]:

Aerosols scatter solar radiation back to space, thus enhancing the planetary albedo and exerting a negative (cooling) climate forcing. Models estimate that the direct cooling effect of anthropogenic sulfate aerosols [e.g., *Charlson et al.*, 1992; *Kiehl and Briegleb*, 1993] may have offset as much as 25% of the greenhouse forcing. Recently, the inclusion of other aerosols (e.g., organics, black carbon, and dust) have shown that the problem is considerably more complex and more important [e.g., *Penner et al.*, 1992; *IPCC*, 1995]. Absorbing aerosols such as black carbon can even change the sign of the forcing from negative to positive [e.g., *Haywood and Shine*, 1997; *Heintzenberg et al.*, 1997; *Liao and Seinfeld*, 1998; *Haywood and Ramaswamy*, 1998]. Observational studies have documented the importance of absorbing aerosols even in remote oceanic regions [e.g., *Posfai et al.*, 1999]. There is now a substantial amount of literature on absorbing aerosols [*Grassl*, 1975; *Clarke and Charlson*, 1985; *Penner et al.*, 1992; *Chylek and Wong*, 1995; *Hobbs et al.*, 1997; *Novakov et al.*, 1997; *Heintzenberg et al.*, 1997; *Kaufman and Fraser*, 1997; *Hobbs*, 1999]. Aerosols also influence the longwave radiation [e.g., *Lubin et al.*, 1996], but the longwave forcing is much smaller than the solar forcing. The longwave forcing of INDOEX aerosols is included in this study.

Aerosols influence the forcing indirectly by altering cloud optical properties, cloud water content, and lifetime. We begin with the first indirect effect, the so-called "Twomey effect" [*Twomey*, 1977], which arises because of the fundamental role of aerosols in nucleating cloud drops. An increase in aerosol number concentration can nucleate more cloud drops, make the clouds brighter [*Twomey*, 1977] and exert a negative forcing. If the available water vapor source is unaltered, the increase in the number of cloud drops will lead to a decrease in the drop size by inhibiting the formation of larger drizzle size drops. The suppression of larger drops can decrease precipitation (drizzle in the case of low clouds) thus increasing cloud lifetime and/or cloud water content, both of which can enhance cloud albedo. This second indirect effect has been observed in a limited set of aircraft studies [*Albrecht*, 1989] and with satellite studies [*Rosenfeld*, 2000]. The global magnitude of the indirect effect is highly uncertain, but can be large enough to offset a large fraction of the entire greenhouse forcing [*IPCC*, 1995].

More recently, model studies [*Hansen et al.*, 1997; *Kiehl et al.*, 1999; *Ackerman et al.*, 2000] have indicated that the solar heating by absorbing aerosols (biomass burning or fossil fuel combustion related soot) can evaporate low clouds (e.g., stratocumulus and trade cumulus); the resulting decrease in cloud cover and albedo can lead to a net warming whose magnitude can exceed the cooling from the direct effect [*Ackerman et al.*, 2000].

The climate forcing due to aerosols is poorly characterized in climate models, in part due to the lack of a comprehensive global database of aerosol concentrations, chemical composition and optical properties. The uncertain role of aerosols in climate is one of the major sources of uncertainties in simulations of past and future climates. A primary goal of INDOEX [*Ramanathan et al.*, 1995, 1996] is to quantify the direct and the indirect aerosol forcing from observations. This paper addresses the climate effects of the haze over the Indian Ocean and South and Southeast Asia (hereafter referred to as the Indo-Asian haze). The following aerosol field experiments preceded INDOEX.

The overall goals of the Aerosol Characterization Experiment (ACE 1) [*Bates et al.*, 1998] and (ACE 2) [*Raes et al.*, 2000] are to reduce the uncertainty in the calculation of climate forcing by aerosols and to understand the multiphase atmospheric chemical system sufficiently to be able to provide a prognostic analysis of future radiative forcing and climate response [*Bates et al.*, 1998]. ACE 1 took place in the minimally polluted Southern Hemisphere marine atmosphere, and ACE 2 took place over the subtropical northeast Atlantic [*Raes et al.*, 2000].

Smoke, Clouds, Aerosols, Radiation-Brazil (SCAR-B) [*Kaufman et al.*, 1998], a comprehensive field project to study biomass burning, smoke, aerosol and trace gases and their climatic effects, took place in the Brazilian Amazon and cerrado regions during 1995.

The Tropospheric Aerosol Radiative Forcing Observational Experiment (TARFOX) [*Russell et al.*, 1999] was designed to reduce the uncertainty in predicting climate change due to aerosol effects and took place over the United States eastern seaboard during 1996 [*Hobbs*, 1999; *Russell et al.*, 1999].

INDOEX gathered data on aerosols and tropospheric ozone chemistry over the tropical Indian Ocean. The primary aerosol-related objectives of INDOEX are to estimate the direct and the indirect forcing of aerosols on climatologically significant timescales and space scales; link the forcing with the chemical and microphysical composition of the aerosols; and evaluate climate model estimates of aerosol forcing. This paper describes the major findings that resulted from the aerosol objectives. The results presented here are for a heavily polluted and a poorly understood region of the planet. It establishes the Indo-Asian haze as an important phenomenon with

global climate implications. The added significance is that this oceanic region borders on rapidly developing, heavily populated nations with the potential for large increases in the future.

The INDOEX observations were made over the tropical Indian Ocean during the Northern Hemisphere dry monsoon (December to April). Since 1996, an international group of scientists has been collecting aerosol, chemical and radiation data from ships, satellites and surface stations [e.g., *Krishnamurti et al.*, 1998; *Jayaraman et al.*, 1998], which culminated in a major field experiment with five aircraft, two ships, several satellites and numerous surface observations conducted during January through March, 1999 (Plates 1a and 1b). In addition to these platforms, the European Meteorological Satellite Organization moved the geostationary satellite, METEOSAT-5, over the Indian Ocean to support the INDOEX campaign. The first field phase (FFP) took place during February and March 1998, and the intensive field phase (IFP) took place from January through March 1999.

The tropical Indian Ocean provides an ideal and unique natural laboratory to study the role of anthropogenic aerosols in climate change. This is probably the only region in the world where an intense source of anthropogenic aerosols, trace gases and their reaction products (e.g., ozone) lies juxtaposed to the pristine air of the Southern Hemisphere [*Ramanathan et al.*, 1996; *Krishnamurti et al.*, 1998]. The polluted and pristine air are connected by a cross equatorial monsoonal flow into the Intertropical Convergence Zone (ITCZ), which, during INDOEX, was located between the equator and about 12°S. The monsoonal flow from the northeast to the southwest (Plate 2b) brings dry continental air over the ocean which leads to a low level temperature inversion, mostly clear skies with scattered cumuli (see the dark and light blue shaded regions in Plate 2a) and minimal rain, all of which enable the haze laden with pollutants to accumulate and spread on an ocean basin scale.

The results and analyses presented in this paper are unique in many respects. It integrates observations taken simultaneously from several platforms (Plates 1a and 1b): top-of-the atmosphere data collected by several satellites; in situ data from the Hercules C-130 and the Citation aircraft; surface and column data from the R/V *Ron Brown* and the R/V *Sagar Kanya*; surface and column data from the Kaashidhoo Climate Observatory (KCO) at 4.97°N, 73.5°E, in the Republic of the Maldives; remotely measured data from a multiwavelength-lidar station at Male (4.18°N, 73.52°E) in the Republic of Maldives; and the INDOEX French stations at Goa (15.45°N, 78.3°E) and Dharwad (15.4°N, 75.98°E). These data are integrated with a Monte Carlo Aerosol-Cloud Radiation (MACR) model, satellite-derived aerosol regional distribution over the ocean and a four-dimensional aerosol assimilation model for the land regions [*Collins et al.*, 2001]. The direct forcing under clear skies has been documented by *Satheesh and Ramanathan* [2000] for the KCO location and by *Rajeev and Ramanathan* [2001] for the entire tropical Indian Ocean. This paper takes on the more challenging topics dealing with the direct forcing in cloudy skies and the indirect forcing. This paper focuses on the IFP period of January–March 1999. However, the conclusions of this INDOEX study should be applicable to other years as well. For example, analyses of satellite data for 1996 to 2000 [*Tahnk*, 2001] reveal that the seasonally (January–March) and the spatially averaged (0° to 30°N) aerosol optical depths for these 5 years vary by less than 10% of the 1999 value shown here.

2. Integration of Field Observations With Satellites and Models

A schematic of the integration scheme is shown in Plate 3. The platforms (Plates 1a and 1b) were designed to accomplish two distinctively different objectives: process or "closure studies" and "gradient studies." Focusing on the C-130 flight tracks shown in Plate 1b and 2b, flights for the process studies were directed from Male toward the northern Arabian Sea to understand the composition of aerosols and other gaseous pollutants close to their sources; process flights were also undertaken southward from Male to understand the aerosol composition far away from the source regions. Next, long transequatorial flights ("gradient flights") from Male to about 10°S were undertaken to estimate the horizontal gradient of aerosol concentration, aerosol composition, radiation fluxes, cloud condensation nuclei and drop concentration. In view of the significant daily and seasonal variability in aerosol concentrations, we need continuous measurements through the year. For this purpose, during 1998, we established KCO on the island of Kaashidhoo, in the Republic of the Maldives, about 500 to 1000 km downwind of major cities in the subcontinent (Plate 1b). The island is about 3 km long and slightly more than 1 km wide, isolated from the nearby islands (about 20 km from the nearest Maldivian island) and about 500 km away from the nearest mainland, the Indian subcontinent. The population of the island is about 1600 and is free from anthropogenic activities such as industry or automobile transport. The observatory is located on the northeast tip of the island so that the local pollution, e.g., biomass burning on the island, is naturally restricted at the observatory since the synoptic-scale winds are mostly from the northeast during the period of interest.

In the remainder of this section we summarize the process (closure) studies, we introduce MACR, which was developed in part based on the process study philosophy, we then review the gradient studies, and finally review how MACR will be used to determine the direct and the first indirect radiative forcing.

Near-continuous measurements were maintained at KCO for aerosol chemical composition, size distribution, spectral optical depths, vertical distribution of aerosol extinction coefficient (by multispectral Lidar), cloud condensation nucleus (CCN) spectra and radiation fluxes. These data were used to link aerosol optical depth and direct aerosol forcing with aerosol chemical composition and microphysical properties; link aerosol concentration with CCN for a wide variety of low and heavily polluted conditions; and develop an aerosol optical model that agrees with surface measurements of scattering, absorbing coefficients and aerosol humidity growth factors. Aircraft data were then used to get a better representation of the vertical distribution of aerosol composition, CCN and microphysical properties. These data were then incorporated in MACR to obtain the forcing on regional scales.

MACR uses measurements of physical and chemical properties of aerosols as input and estimates radiation fluxes for three-dimensional broken cloud systems with a realistic distribution of atmospheric gases and aerosol species. The cloud parameters, such as cloud base and top heights, are obtained from the C-130, and cloud optical depth is calculated as described in section 8 and Appendix A. The trade cumulus clouds

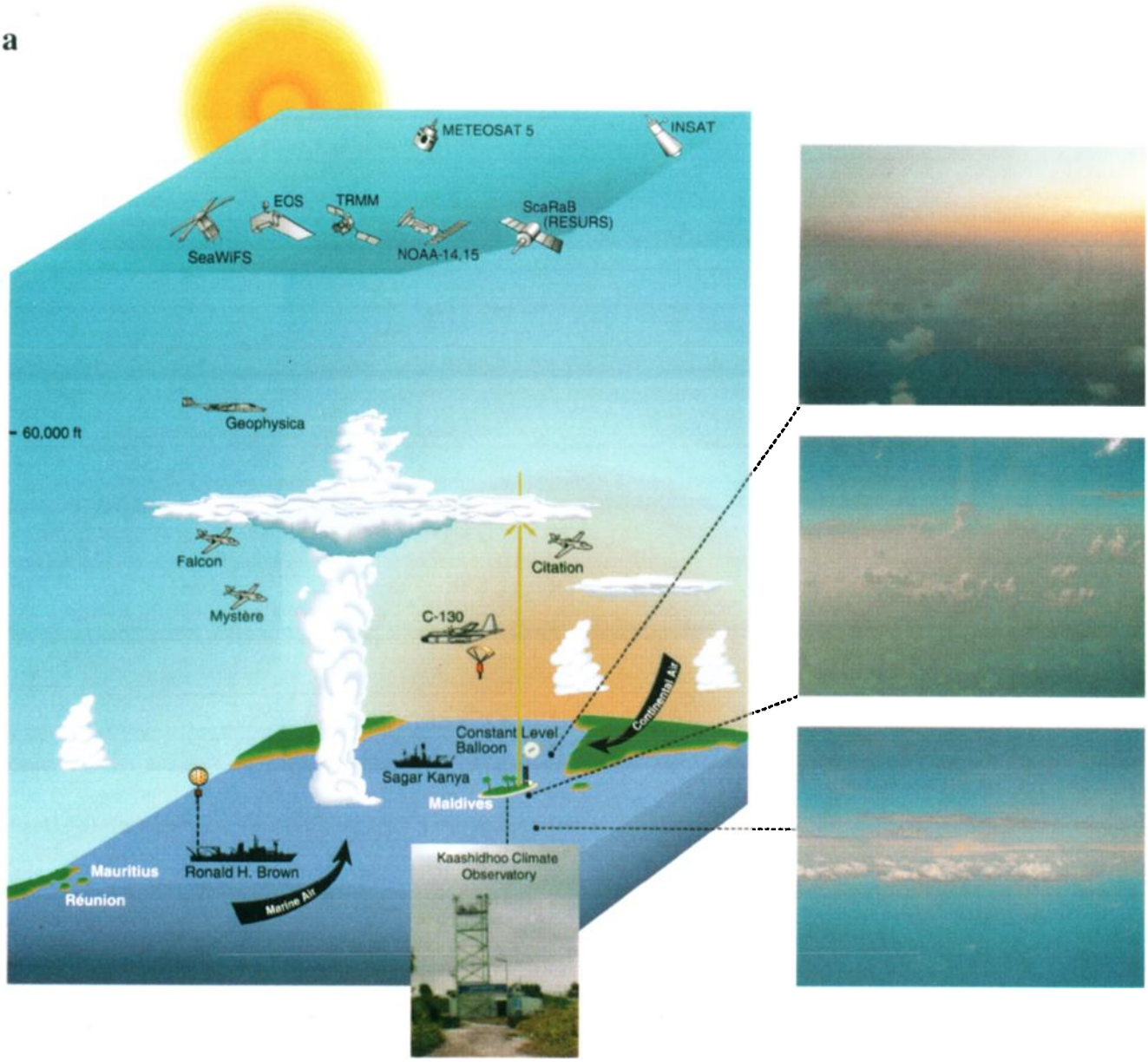

Plate 1. (a) The plate displays two separate but related pieces of information. First is the INDOEX cube showing the various observing platforms, which included satellites, aircraft, ships, balloons, dropsondes, and surface stations at Maldives and India. The three photographs show the pictures of the dense haze in the Arabian Sea, the trade cumuli imbedded in the haze, and the pristine southern Indian Ocean. (b) This illustration of the INDOEX composite observing system shows the domains of the various platforms. Geostationary satellites (METEOSAT-5 and INSAT) and polar orbiters (NOAA 14, 15, and ScaRaB) provide synoptic views of the entire study region. The C-130, the Citation, and the Mystère fly from Hululé in the Maldives, while the Geophysica and the Falcon depart from the Seychelles. These aircraft perform north-south flights from about 10°N to 17°S and east-west flights from about 75°E to 55°E measuring solar radiation fluxes, aerosol properties and distribution, cloud microphysics, chemical species, and water vapor vertical distribution. The ocean research vessels *Ronald H. Brown* and *Sagar Kanya* travel between Goa, Malé, La Réunion, and Mauritius transecting the intertropical convergence zone and sampling surface solar radiation, aerosol absorption and scattering, chemical species, ozone, winds, and water vapor vertical distribution. The *Sagar Kanya* also sails in the source region along the western coast of India. Surface stations in India (including Mount Abu, Pune, and Trivandrum), the Maldives (Kaashidhoo Climate Observatory), Mauritius, and La Réunion measure chemical and physical properties of aerosols, solar radiation, ozone, and trace gases. Closely related to surface platforms, constant level balloons are flown from Goa to track low-level airflow from the subcontinent and measure air pressure, temperature, and humidity.

b

Plate 1. (continued)

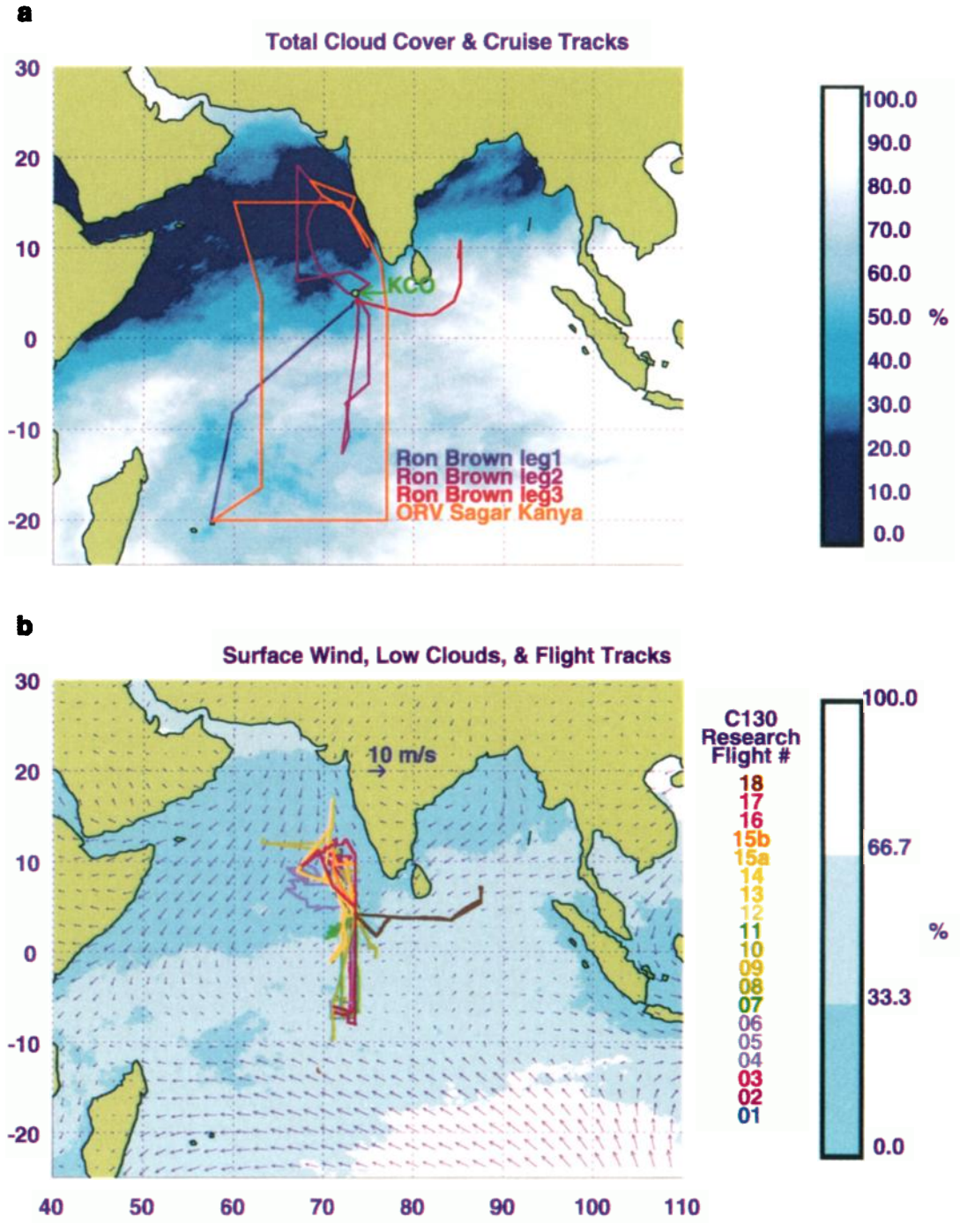

Plate 2. (a) Illustrates the total cloud amounts for January–March 1999 in percent cover over the tropical Indian Ocean. Cloud amount was retrieved from METEOSAT-5 satellite radiances provided by the European Meteorological Satellite Organization (EUMETSAT). The retrieval scheme allows the determination of low clouds, cirrus, cumulus, and anvils. The band of near-overcast cloudiness represents the approximate location of the ITCZ. The orange line represents the track of the R/V *Sagar Kanya* during February and March. The color lines (dark blue, brown, and red) represent the cruise track of R/V *Ron Brown* during late February through the end of March. The green arrow illustrates the location of the Kaashidhoo Climate Observatory. (b) Illustrates the northeasterly to southwesterly monsoonal flow during February 1999 and the low-level cloud amounts. Surface wind data for February were obtained from the National Center for Environmental Prediction/National Center for Atmospheric Research Reanalysis Project. The color lines on the map represent the flight paths of the C-130.

prevalent in this region have horizontal scales of few hundred meters to few kilometers, which we account for through the Monte Carlo radiative transfer modeling [*Podgorny et al.*, 2000]. We use fractal broken cloud scenes to simulate cloud fractions between 0 (clear sky) and 1.0 (overcast sky). The cloud fractions are retrieved once every 30 min from the METEOSAT Infrared (IR) brightness temperature data. MACR adopts three types of sky conditions, specifically, clear

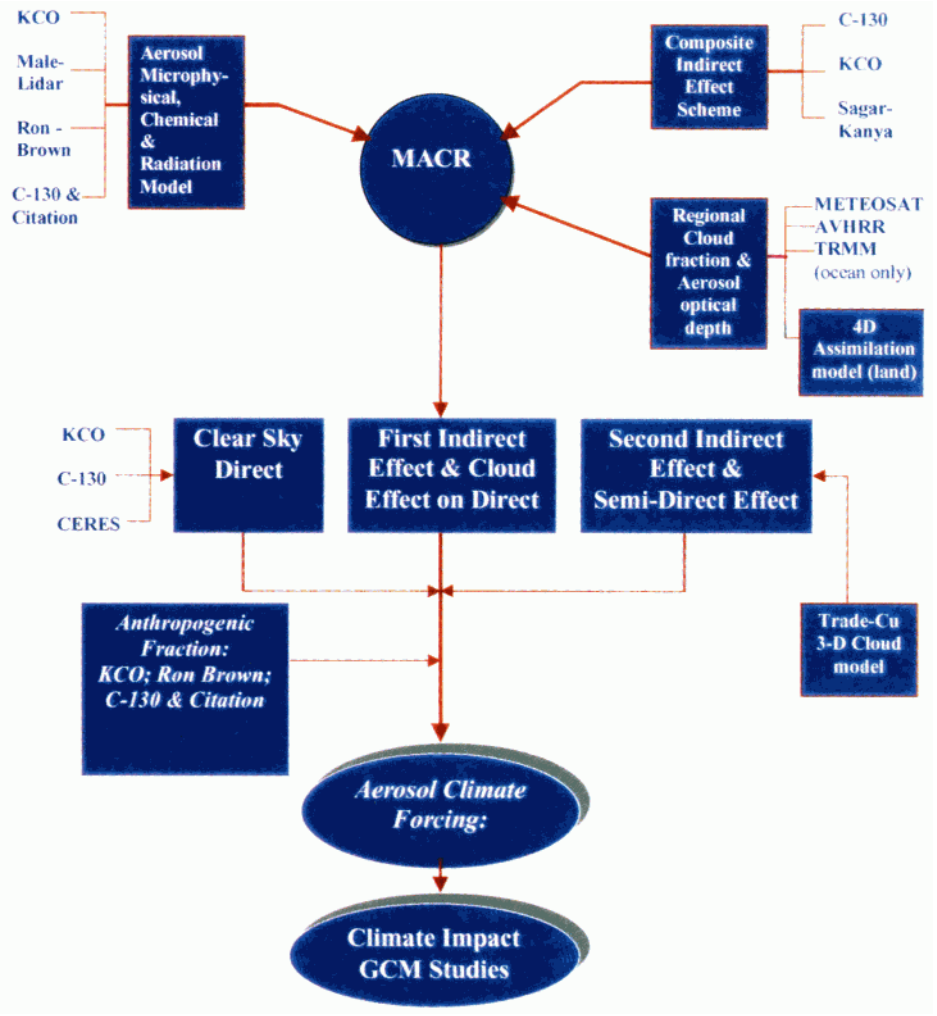

Plate 3. A schematic of the data integration scheme. Central to the integration scheme is the MACR model. The direct forcing in clear skies is obtained directly from observations at KCO, C-130, and the Clouds and Earth Radiation Exchange System (CERES) radiation budget instrument on board the Tropical Rainfall Mapping Mission (TRMM) satellite. The aerosol-chemical-microphysical components of MACR are developed from observations from KCO, the lidar in Male, the R/V *Ron Brown*, the C-130, and the Citation. The dependence of cloud optical properties on aerosol concentration (the so-called first indirect effect) is incorporated in MACR based on the C-130, the KCO, and the R/V *Sagar Kanya* observations. The regional distribution of the forcing is obtained by integrating satellite-retrieved aerosol optical depths and cloud fraction with MACR. The resulting aerosol forcing is inserted in the NCAR-CCM3 to obtain climate impacts.

skies, low clouds (including cirrus), and convective clouds including anvils.

MACR treats each aerosol species explicitly by using the corresponding phase functions and single-scattering albedos for individual species [*Satheesh et al.*, 1999]. The model also accounts for all multiple scattering and absorption by individual aerosol species, air molecules and reflections from the surface. The solar bands from 0.2 to 4.0 μm are divided into 25 narrow bands. Hygroscopic aerosol species (all species except soot, dust and ash) are allowed to grow with relative humidity [*Hegg et al.*, 1993; *Nemesure et al.*, 1995] using radiosonde profiles of water vapor (launched from KCO). The modeled change in aerosol scattering due to growth with relative humidity is compared with observed values in section 6. MACR also accounts for the corresponding changes in scattering phase function. A more detailed description of MACR is given by *Satheesh et al.* [1999] and *Podgorny et al.* [2000].

MACR was used in two modes: First, it was used to retrieve aerosol optical depths from satellite data, thus extending in situ data to regional scales. Second, it was used in conjunction with satellite low-cloud data to obtain the regional direct and indirect forcing. For the indirect effect the KCO data were combined with the C-130 data to derive a composite indirect effect scheme (described in Appendix A) that relates CCN, effective supersaturation and effective cloud drop radius with aerosol number density. In order to obtain regional forcing values as a function of longitude and latitude from these point source estimates, we use the advanced very high resolution radiometer (AVHRR) data collected from the polar orbiting NOAA satellite to retrieve aerosol optical depths (AODs), and the METEOSAT data for cloud fraction.

The long transequatorial flights of the C-130 (Plate 2b) and the cruise by the R/V *Ron Brown* (Plate 2a) established the sharp north-south gradients in aerosols, CCN and aerosol

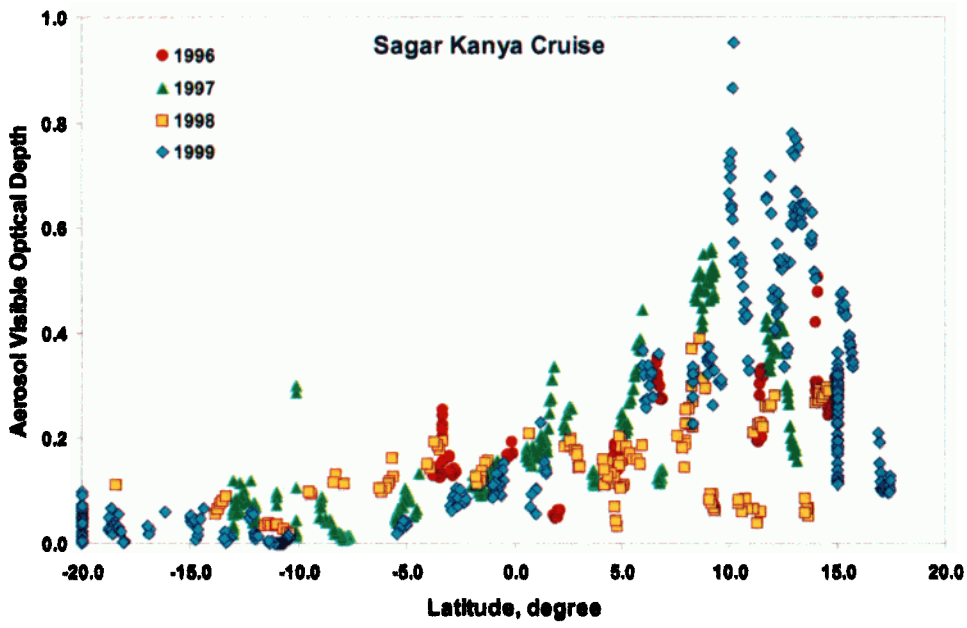

Plate 4. The latitudinal variation of τ_v (0.5 μm) measured by the Indian research vessel *Sagar Kanya* during 1996 to 1999. The multiwavelength Sun photometer used for this data is described by *Jayaraman et al.* [1998]. The precision of the measurement is ±0.03 or 20%, whichever is smaller. Each color represents a different year.

chemical composition. These gradients were used to evaluate the prediction of models for the composite indirect effect scheme. These transequatorial gradient data were also used to estimate the anthropogenic contribution to the aerosol forcing.

The steps for estimating clear-sky direct forcing by aerosols have been documented extensively in the open literature [*Satheesh et al.*, 1999, hereafter referred to as S99; *Rajeev et al.*, 2000; *Conant*, 2000; *Collins et al.*, 2001; *Rajeev and Ramanathan*, 2001] and are briefly summarized below. We adopt the following convention with respect to aerosol optical depths: τ_a refers to aerosol optical depths at 0.5 μm; and τ_v refers to the aerosol optical depth at 0.63 μm.

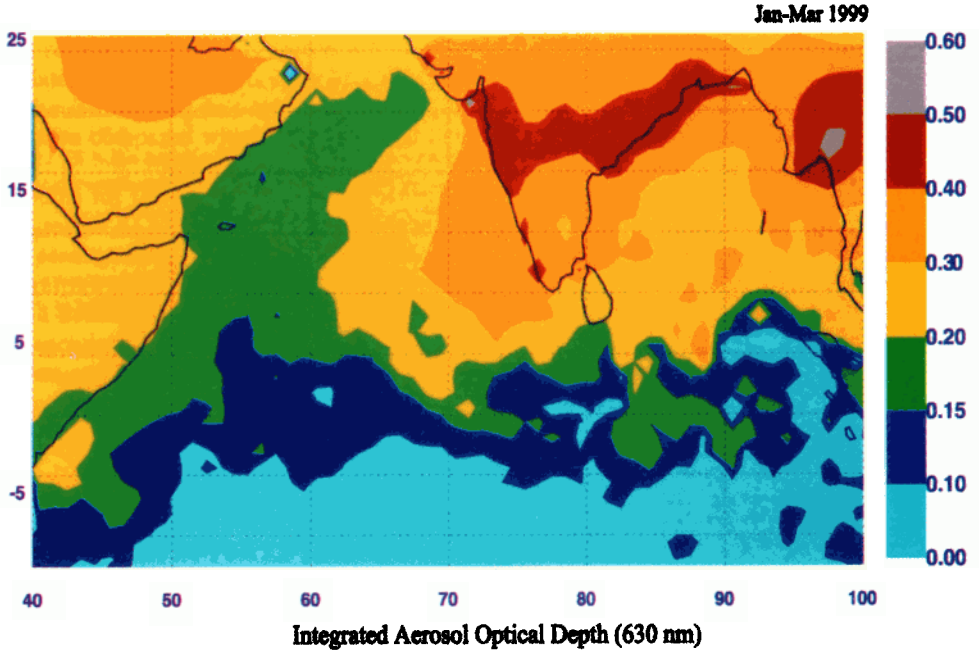

Plate 5. The regional map of aerosol visible optical depth τ_a. The τ_a values over ocean are retrieved from AVHRR data [*Rajeev et al.*, 2000] and over land are estimated using a 4-D assimilation model [*Collins et al.*, 2001]. The figure illustrates the north-south gradient in τ_a with values around 0.5 around the coast and less than about 0.1 south of the equator. As described by *Rajeev and Ramanathan* [2001], the standard error of the seasonal averages shown in this plate is about ±0.02 or 15%, whichever is greater.

1. The in situ data for size-resolved aerosol chemical composition; microphysics and vertical profile were used to develop an aerosol microphysical model (S99). The single-scattering albedo and the spectral variation in the column aerosol optical depth (AOD) simulated by this model were verified with multiwavelength Sun photometer measurements of AOD at KCO.

2. The aerosol model was employed in MACR to simulate the solar radiation fluxes, which were validated with radiometric measurements deployed at the surface at KCO and the TRMM satellite.

3. The MACR aerosol model was used to retrieve aerosol visible optical depth τ_v from satellite radiances in the 0.63 μm region. We use 0.63 μm region since this is the central wavelength of the satellite radiance used for retrieving the optical depth. It should be noted that $\tau_a \approx 1.30\ \tau_v$.

4. The retrieved τ_v was validated with τ_v measured by Sun photometers deployed at the surface and aboard ships [*Rajeev et al.*, 2000]. Steps 1–4 yielded τ_v only over the ocean since the surface reflectivities needed in the radiation retrieval models are not well known for land surfaces.

5. For land a four-dimensional (4-D) global aerosol assimilation model developed especially for INDOEX [*Collins et al.*, 2001] was used. This model initializes daily values of satellite-retrieved τ_v for the oceans and aerosol surface emission data for land and uses model winds to advect the aerosol horizontally and vertically. The model predictions were extensively evaluated against data collected during the field campaign.

The cloud and aerosol microphysical data taken at KCO and from the C-130 are used to develop a composite scheme for the first indirect effect. This scheme estimates cloud optical depth as a function of aerosol optical depth. The composite scheme is inserted in MACR, in conjunction with the satellite data for cloud cover and aerosol optical depth, to estimate the regional forcing for the first indirect effect. The details are explained in Appendix A. However, INDOEX observations do not include data on the second indirect effect and the semidirect effect. We include these two effects in our forcing estimates using the model study of *Ackerman et al.* [2000] and *Kiehl et al.* [2000].

In summary, as depicted in Plate 3, the direct forcing and the first indirect effect are obtained directly from INDOEX observations and are described first in sections 7 and 8, respectively. The model-derived forcing values due to the second indirect effect and the semidirect effect are described in section 9. Section 10 uses these results to summarize the various contributions to the aerosol forcing by anthropogenic sources.

3. Space and Timescales of the Haze

Plate 4 shows 4 years of aerosol visible optical thickness data collected from a multispectral Sun photometer [*Jayaraman et al.*, 1998] on board the R/V *Sagar Kanya* during the winter months of 1996 to 1999. The optical depth at a wavelength λ, τ_λ, is defined such that the direct solar beam transmitted to the surface decreases to exp $(-\tau_\lambda/\cos\theta)$ due to aerosol scattering and absorption, where θ is the solar zenith angle. Thus τ_λ quantifies the optical effect of the aerosol column between the surface and top-of-the atmosphere (TOA) at the wavelength λ. Plate 4 shows the optical depth at $\lambda = 0.5$ μm denoted by τ_a. For each of the 4 years there is a steep latitudinal gradient with τ_a increasing from about 0.05 near 20°S to 0.4 to 0.7 around 15°N. Typically, τ_a of 0.05 to 0.1 is considered to be a background value for pristine air (S99), while τ_a in excess of 0.2 are indicative of polluted air. The τ_a frequently exceeded 0.2 north of 5°N, in spite of being at least 500 to 1000 km away from major urban regions. The ship data clearly demonstrate the chronic recurrence of the haze. The interannual variability is also large. At KCO, for example, τ_a during 1999 was more than a factor of 2 greater than in 1998. However, the interannual variability of the spatially averaged τ_a is much smaller.

Upon integrating the in situ and satellite measurements with the MACR model and the 4-D assimilation model [*Collins et al.*, 2001], we discovered that during the winter months the thick haze layer spreads over most of the northern Indian Ocean (NIO) and over most of the Asian continent (Plate 5). The τ_a exceeds 0.25 over the eastern Arabian Sea and most of the Bay of Bengal; and exceeds 0.4 over most of South and Southeast Asia. There is a sharp transition to background values between 5°S to 8°S because of the ITCZ, which restricts interhemispheric transport. The fact that the haze can reach as far south as 5°S is also captured in the Transmission Electron Microscope image of particles (Figure 1) from the C-130. The soot particle is shown attached to the aerosol collected at 6.1°S, more than 1500 km from the source. The cause of the large-scale spread of the haze is demonstrated from the trajectories of the constant level balloons launched from Goa, India. Seventeen overpressure (constant volume) balloons were launched between January 16 and February 28, 1999. They followed quasi-isopycnic trajectories, except for eventual occurrence of diurnal oscillations in the vertical, due to occasional water loading of the envelope. Their nominal levels were comprised between 960 and 810 hPa. The northeasterly flow was clearly evident in most of the trajectories. Most of the balloons survived the flight to the ITCZ. The travel time across the Arabian Sea to the equator was about 3 to 7 days. Because of the scarcity of rain during the northeast monsoon, the lifetime of the aerosols is of the order of 10 days [*IPCC*, 1995], and the haze spreads over the whole NIO.

The seasonal cycle of τ_a is obtained from KCO. The dry monsoon begins around November and initiates the buildup of the haze from the premonsoonal daily mean values of 0.05 to 0.1 to values as high as 0.9 in late March. The same seasonal cycle has been observed over western India by the stations at Goa and Dharwad [*Leon et al.*, this issue]. The transition to the southwest monsoon begins in April after which the pristine Southern Hemisphere air replaces the haze.

4. Chemical, Microphysical, and Optical Properties: Anthropogenic Contribution

4.1. Chemical

Aerosol optical and chemical measurements were performed on board the C-130, the R/V *Ronald H. Brown*, and from KCO at 5°N, 73.5°E. At KCO we measured the size distribution and chemical composition of fine particles, collected on filters and cascade impactors [*Chowdhury et al.*, this issue]. The chemical data summarized in Plate 6 are taken from *Lelieveld et al.* [2001]. The filter analysis shows an average mass concentration of nearly 17 μg m^{-3} (Plate 6). The aerosol composition was strongly affected by both inorganic and organic pollutants, including black carbon (soot). Very similar results were obtained from boundary layer flights by the C-130 aircraft and from the R/V *Brown*, indicating that the aerosol composition was quite uniform over the northern Indian Ocean.

The measurements show that the fine aerosol (dry mass at

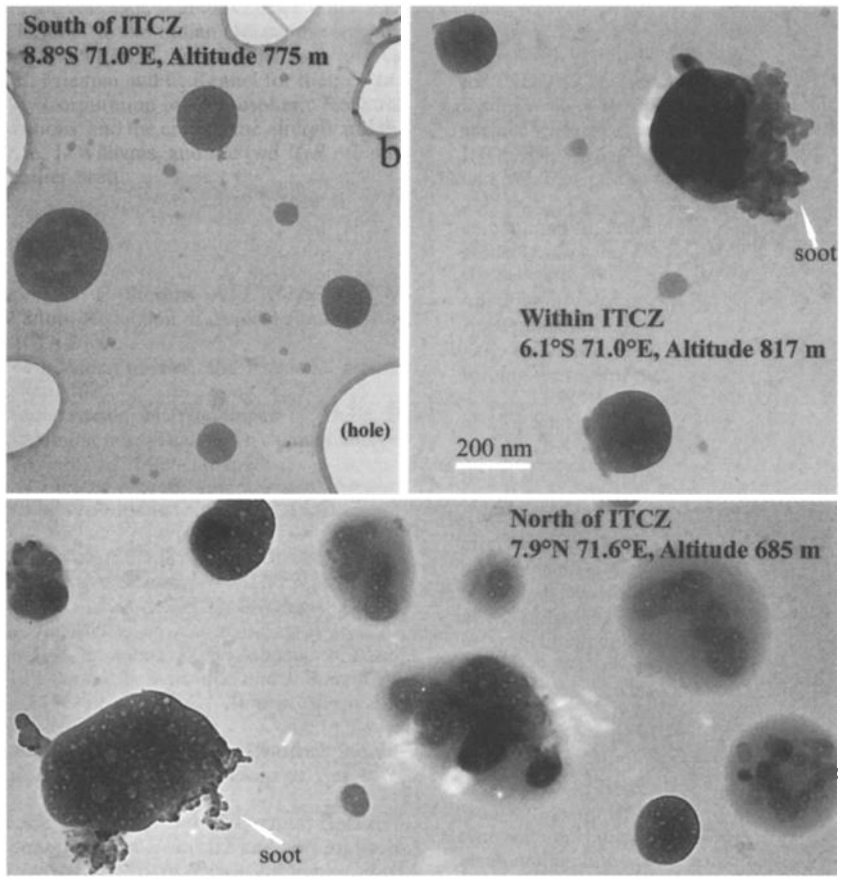

Figure 1. Transmission Electron Microscope (TEM) images of aerosols south of the ITCZ (top left), within the ITCZ (top right), and north of the ITCZ (bottom). It can be seen that the soot is associated with sulfate/organic aerosols in the Northern Hemisphere and one is found as far as 6°S. The soot, while it seems to be attached to the surface of the aerosol, may have been ejected to the surface from the core because of the location in the TEM. The location and altitude of the measurement is included in each panel. All the measurements are between approximately 690 and 820 m altitude.

diameters <1 μm) was typically composed of 32% sulfate, 26% organic compounds, 14% black carbon (BC), 10% mineral dust, 8% ammonium, 5% fly ash, 2% potassium, 1% sea salt, and trace amounts of methyl sulfonic acid (MSA), nitrate, and minor insoluble species (Plate 6b). The coarse aerosol (dry mass at diameters between 1 and 10 μm), as observed at KCO, typically consisted of 25% sulfate, 11% mineral dust, 19% organic compounds, 12% sea salt, 11% ammonium, 10% BC, 6% fly ash, and 1% potassium. Interestingly, at KCO the coarse aerosols also contained about 4% nitrate, while farther north, as observed by the C-130 aircraft, this was even 7%, substantially more than the nitrate in the fine aerosols. This suggests that nitric acid from the gas phase preferentially partitions into the coarse particles.

The fine particle (particles smaller than 1 μm diameter) concentrations observed over the Indian Ocean are comparable to urban air pollution in North America and Europe that reduces air quality [*Christoforou et al.*, 2000]. Moreover, the high BC concentration gives the aerosol a strong sunlight absorbing character. The KCO impactor measurements show a dry particle size distribution that peaks at about 0.5 μm physical diameter. In this size range the sulfate aerosol (and associated ammonium) contribute most to the light scattering. The peak BC concentration occurred at 0.3–1.0 μm physical diameter, larger than typically found in cities like Los Angeles (e.g., 0.1–0.2 μm from fresh engine exhaust from *Kleeman et al.* [2000]; and 0.2–0.4 μm in ambient Los Angeles air from *Kleeman et al.* [1997]). Mass spectrometric single-particle analysis shows that the BC particles were always mixed with organic compounds and sulfate, indicating substantial chemical aging and accumulation of gas-to-particle conversion products. This may partly arise from the processing by scattered cumulus clouds (i.e., condensation, coalescence, and evaporation of droplets; sulfate formation within BC-containing droplets). The prevalence of such clouds is shown in Plate 2b.

The BC aerosol and the fly ash, as observed during INDOEX, are unquestionably human-produced since natural sources are negligible [*Cooke et al.*, 1999; *Novakov et al.*, 2000]. Likewise, non-sea-salt sulfate can be largely attributed to anthropogenic sources. The filter samples, collected on board the R/V *Brown* in the clean marine boundary layer south of the ITCZ, reveal a fine aerosol sulfate concentration of about 0.5 $\mu g\ m^{-3}$, probably from the oxidation of naturally emitted dimethyl sulfide. Considering that the sulfate concentration over the northern Indian Ocean was close to 7 $\mu g\ m^{-3}$, we infer an anthropogenic fraction of about 90%. Similarly, the ammonium concentration south of the ITCZ, from natural ocean emissions, was 0.05 $\mu g\ m^{-3}$, indicating an anthropogenic contribution of 97% to the nearly 2 $\mu g\ m^{-3}$ of ammonium observed north of the ITCZ.

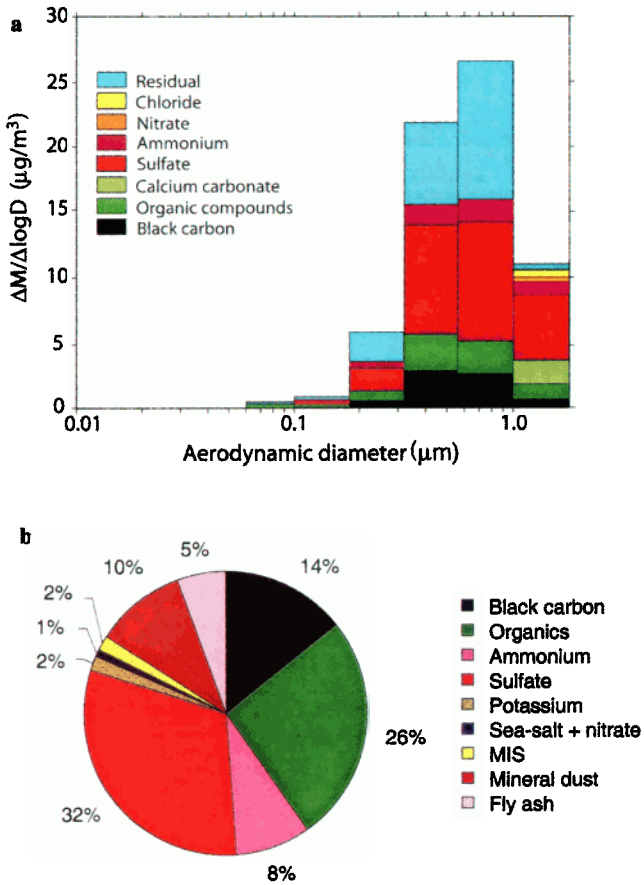

Plate 6. (a) Average chemical composition of fine aerosol on KCO (Maldives) as a function of particle size for February 1999 (total mass 17 $\mu g\ m^{-3}$). The residual includes mineral dust, fly ash, and unknown compounds. For gravimetric mass determination the average precision of the impactor measurements, calculated from the nominally four replicate impactor samples taken each event, was found to be ±5.3% for samples greater than or equal to 2.0 $\mu g\ m^{-3}$, and ±22.5% for samples less than 2.0 $\mu g\ m^{-3}$ whose values were still significantly greater than zero. For sulfate, ammonium ion, organic matter, and elemental carbon the average precision of the measurements based on repeated analysis of standard solutions was ±2.3%, ±5.4%, ±11.1%, and ±5.9%, respectively, for samples greater than or equal to 0.2 $\mu g\ m^{-3}$; for samples smaller than 0.2 $\mu g\ m^{-3}$ the average precision was ±16.4%, ±12.4%, ±18.4%, ±34.9%, and ±12.4%, respectively. These precision values represent ±1 standard error of the determination of a single impactor sample. Plate 6a is constructed from the average of eight impactor sampling events, so the standard error of the means calculated from those eight samples is correspondingly smaller. (b) Average mass fractions of aerosol ($D < 1$ μm) as observed from the C-130 aircraft during February and March 1999 (total mass 22 $\mu g\ m^{-3}$). Thirty-four boundary layer samples are included in the averages. MIS is minor inorganic species (reproduced from *Lelieveld et al.* [2001] with permission from the authors and *Science*). When we account for spatial and temporal variability, instrumental precision, and the number of samples, our estimate for the overall standard error of the averages shown in Plates 6a and 6b is about ±20%.

It is more difficult to attribute the organic aerosol fraction to a particular source category. However, the BC/total carbon ratio of 0.5, as derived from the filter samples, points to fossil fuel combustion as the main contributor [*Novakov et al.*, 2000]. In the aerosol south of the ITCZ, organic compounds were negligible, whereas over the northern Indian Ocean it was almost 6 $\mu g\ m^{-3}$. We thus infer that most (at least 90%) of the particulate organics north of the ITCZ were of anthropogenic origin. INDOEX fine aerosol components of natural origin included a total mass fraction of 1% sea salt and 10% mineral dust. However, some of the mineral aerosol likely originated from road dust and agricultural emissions during the dry monsoon, so that the 10% assumption for the natural dust represents an upper limit. Taken together, the human-produced contribution to the aerosol over the northern Indian Ocean was about 80% (±10%). Note that these aerosol mass fractions, in conjunction with Plate 6b, have been used to perform the optical depth calculations.

The following additional considerations also justify our conclusion that anthropogenic sources contribute a major fraction (80%) to the aerosol loading. The observed BC/total carbon ratio of 0.5 and the sulfate/BC ratio of 2–2.5 are both more typical for fossil fuel derived aerosol than for biomass burning aerosol [*Novakov et al.*, 2000]. The substantial mass fraction of sulfate in the aerosol supports this analysis since SO_2 emissions are dominated by fossil fuel use. Important information about aerosol sources is provided by the comparison of potassium (K^+, mostly from biomass burning) with sulfate (mostly from fossil fuel combustion). The K^+/BC ratio in INDOEX aerosol was about 5 times smaller than that typically found in biomass smoke [*Novakov et al.*, 2000]. As concluded by *Novakov et al.* [2000], fossil fuel related emissions of BC and sulfur are the major contributors (at least 70%) to the aerosols over the Indian Ocean. Fossil fuel related emissions are not very efficiently removed near the sources since it takes several days to convert SO_2 into sulfate and BC into hygroscopic particles. Therefore the dry monsoon can carry these compounds across the Indian Ocean where they contribute to light extinction.

4.2. Optical

The scattering and absorption of solar radiation by aerosols are governed by the chemical composition, the size distribution, and the number density. The total number of particles varies from about 250 cm^{-3} in the unpolluted southern Indian Ocean (SIO) air to 1500 cm^{-3} or more in polluted NIO air (Plate 7a). Particles of diameters from a few nanometers (nm) to a few micrometers (μm) contribute to the total number density, but those between 0.05 and 2 μm contribute more than 90% to τ_a. The C-130 data (Plate 6b) account for only fine particles, i.e., diameter $D < 1$ μm. The coarse particles ($D >$ 1 μm) are primarily sea salt and dust, which contribute more than 30% to the mass but less than 10% to τ_a since they are too few. In MACR we use surface measurements at KCO to account for the coarse particles.

The chemical composition determines the refractive index, which, in conjunction with solutions of the Maxwell's equations, yields the scattering and the absorbing cross sections for a single particle of diameter D. The calculated light extinction agrees with direct optical measurements both at KCO and on board the C-130 aircraft across the entire measurement domain down to the ITCZ. The results indicate a remarkably large absorption component of the aerosol, yielding a single-scattering albedo at ambient relative humidity of about 0.9 (discussed later in more detail). The contribution of various constituents to the columnar τ_a is shown in Plate 8 (see S99 for details). The aerosol single-scattering albedo is wavelength-dependent. MACR integrates these solutions with the particle

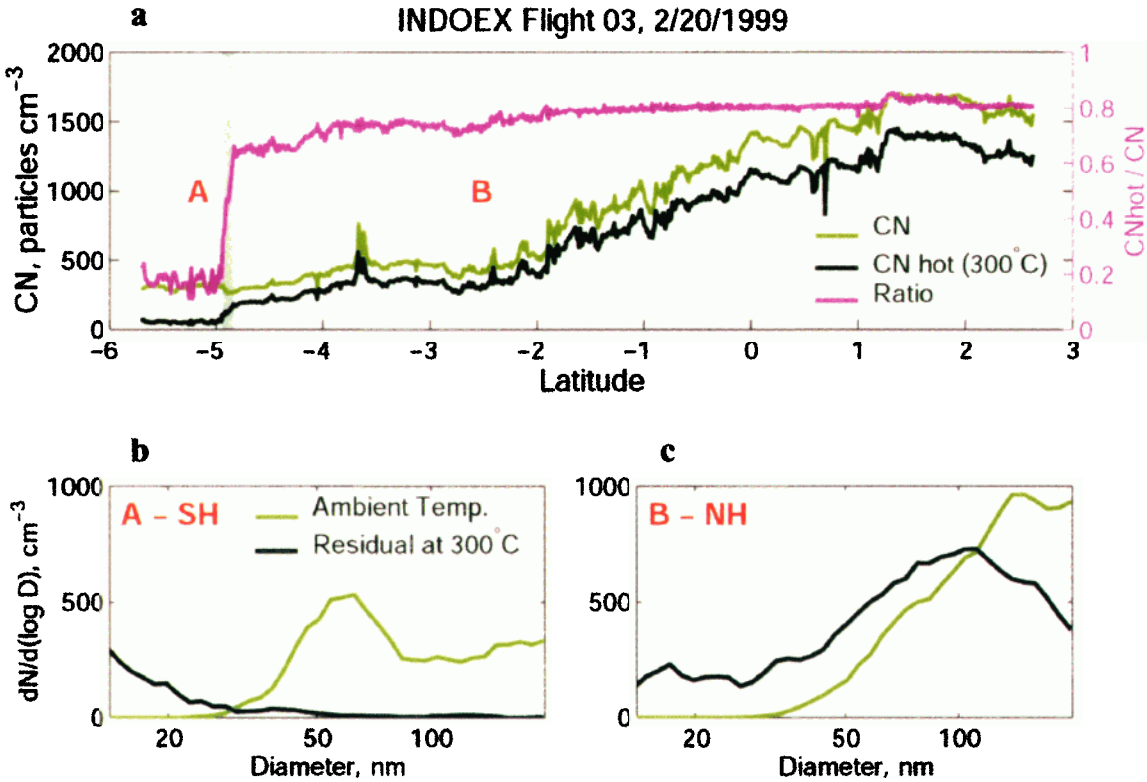

Plate 7. (a) Latitudinal variation of the condensation nuclei (CN) measured during the C-130 flight. Total CN (green curve) and CN_{hot} (black curve, samples collected with a preheater at 300°C) are shown with their ratio (pink curve). This ratio is the nonvolatile fraction of particles remaining after volatile components are removed. The high gradient in total CN number from north to south and the rapid drop in the CN nonvolatile fraction upon crossing the ITCZ (approximated by vertical line) are clearly seen in the plate. Flow errors for the CN counter are <=3%. Particles larger than about 15 nm are counted with high efficiency. The heated inlet was maintained at 300 ±2°C. (b) and (c) Size distributions of dried aerosol and the residual component after heating, as measured with a Differential Mobility Analyzer (DMA). The Southern Hemisphere (SH) distribution (Plate 7b) shows a typical clean marine aerosol, with a dip at 100 nm due to cloud processing (a "Hoppel minimum") and very small amounts of refractory material, while the Northern Hemisphere (NH) plot (Plate 7c) reveals larger particles with much greater refractory parts typical of the INDOEX haze. Errors in overall particle number and particle sizing are <10%.

size distribution and vertical distribution (Plate 9, to be discussed later) and sums up the contributions from all of the altitudes to obtain Plate 8, which enables us to determine the anthropogenic contribution to the radiative forcing.

The percent contribution shown in Plate 8 differs somewhat from the KCO values shown by S99 since the latter is based on surface data for one location (that too for 1998), whereas the present values integrate surface data with in situ values (C-130 data) and for a much larger domain. The anthropogenic contribution to the column τ_a (values are reported here only at 0.5 μm) is about 80% (±10%). While the individual contributions are broken down by species (using MACR), the aerosol time-of-flight mass spectrometer data [*Coffee et al.*, 1999] revealed that these species do not occur as separate particles, i.e., as pure sulfate or pure organic aerosols. Instead, substances are mixed within individual particles as imaged in Figure 1 which shows the soot attached to a sulfate and organic aerosol. MACR allows for this by treating two extreme cases: an externally mixed particle in which each substance occurs as a separate particle; and an internally mixed aerosol in which each particle contains a mixture of all the substances. The difference between the two cases was less than 10% in the calculated τ_a and the forcing, consistent with earlier findings [S99; *Pilinis et al.*, 1995]. Our confidence in the MACR treatment of the radiative effects of the INDOEX aerosols is derived from the fact that the solar fluxes and the clear-sky direct forcing estimated by MACR is in excellent agreement with the observed values (described in section 6). However, the aerosol mixing state can exert a significant role on the indirect effect.

5. Role of Black Carbon in the Forcing

We highlight the role of black carbon because of its major role in the surface and the atmospheric forcing [*Podgorny et al.*, 2000]. The estimates of aerosol forcing prior to 1990 often used assumptions on the imaginary part of the refractive index due to lack of adequate measurements. From the beginning of this decade, more attention has been devoted to the absorbing aerosols [*Penner et al.*, 1992; *Haywood and Shine*, 1997; *Heintzenberg et al.*, 1997; *Hansen et al.*, 1997]. The aerosol forcing also depends on the altitude level at which the aerosol is located and whether the aerosol is above or below clouds [e.g., *Heintzenberg et al.*, 1997; *Haywood and Shine*, 1997]. While the role of absorbing aerosols is enhanced at higher altitudes,

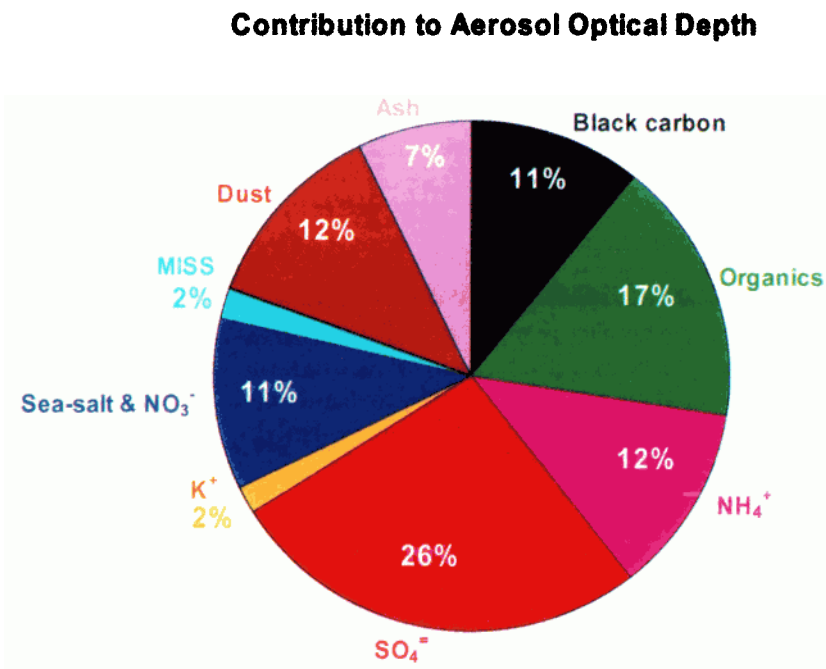

Plate 8. Relative contributions of the various chemical species to τ_a (0.5 μm). When we account for spatial and temporal variability, the standard error of the mean values is about ±15% (relative error). The size distribution of aerosols shows an effective radius of ~0.34 μm. The value of Angstrom coefficient varies from 1.0 to 1.2.

particularly if above clouds, the role of sulfate decreases due to humidity effects [*Heintzenberg et al.*, 1997]. This is where the importance of simultaneous measurements of vertical profiles and absorption properties comes into play.

A key parameter in this regard is the single-scattering albedo (SSA), $\omega = C_s/(C_s + C_a)$, where C_s is the scattering coefficient and C_a is the absorption coefficient. Measured $C_s + C_a$ are shown in Plate 9a for an aerosol layer imbedded in the

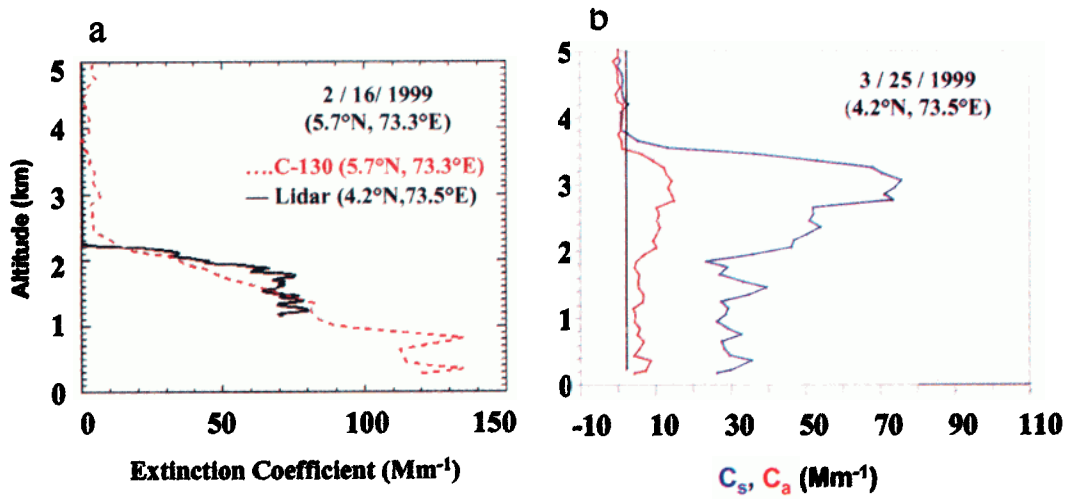

Plate 9. (a) Typical profiles of a "boundary layer aerosol." The data are for the aerosol extinction coefficient (scattering plus absorption). The C-130 data include only submicron particles, and the lidar includes all particles. This difference contributes in part to the difference between the two profiles; the other causes include spatial gradients in the profiles and instrumental uncertainties. (b) Typical "elevated aerosol layer." The data are for scattering (C_s, blue curve) and absorption coefficients (C_a, red curve) measured from the C-130. The C_s is measured with an integrating nephelometer. C_a is measured with a continuous light absorption photometer. Since the C-130 inlet restricts larger particles (diameter >1 μm), the values below 1 km may be uncertain by as much as a factor of 2. Uncertainty in the lidar data is 20% below 2 km and is 30% above 2 km. Uncertainties are greatly reduced when simultaneously measured Sun photometer AODs can be used to constrain the columnar integral of $C_s + C_a$.

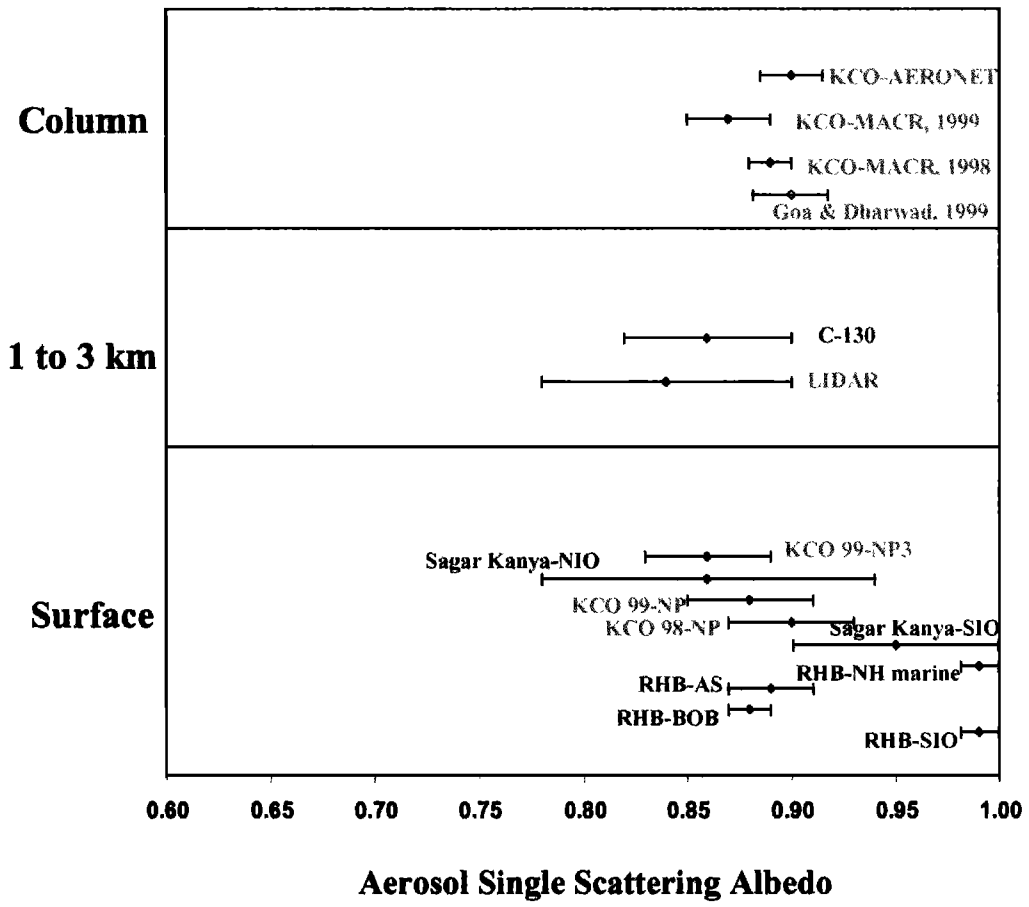

Plate 10. The estimates of aerosol single-scattering albedo ω at $\lambda = 0.53$ μm from various platforms which include the KCO, the C-130 aircraft, the R/V *Sagar Kanya*, and the R/V *Ronald H. Brown* (RHB). The horizontal bar represents uncertainties due to variability and instrumental errors. (bottom) Surface measurements from KCO and ships. KCO-AERONET stands for Aerosol Robotic Network measurements at KCO; KCO-NP3 stands for three wavelength nephelometer and PSAP measurements at KCO; NP stands for single wavelength nephelometer and PSAP; AS stands for Arabian Sea; and BOB stands for Bay of Bengal. (middle) Measurements between 1 and 3 km from the C-130 aircraft and lidar. (top) Column-integrated values estimated using MACR and retrieved from the sky radiance measurements using the Sun photometer and radiometer at KCO. The aerosol single-scattering albedo is wavelength-dependent. First set is the direct measurements by a nephelometer and a photometer, in which the aerosol-laden air is drawn into the instrument. The second method employs a lidar [*Althausen et al.*, 2000] at Male. The data measured with the multiwavelength lidar are used to determine the backscatter coefficient at six wavelengths and the extinction coefficient at two wavelengths independently and simultaneously. From these eight spectral data, physical parameters of the aerosol size distribution and the complex refractive index are calculated using an inversion algorithm, which are then used for the calculation of ω. The third method employs the measured mass, composition, and size distribution of the aerosol (Plate 6) in conjunction with a Mie-scattering model (solution of Maxwell's equation for a spherical particle) to determine the aerosol radiative properties (Plate 8), averaged over the vertical column.

boundary layer, and measured C_s and C_a are shown separately in Plate 9b for an elevated aerosol layer. The boundary layer aerosol profile occurred about 1/3 of the time, and the elevated profile occurred about 2/3 of the time. The coalbedo, $\alpha = (1 - \omega)$, is the basic measure of light absorption. In the visible spectrum, α ranges from about less than 0.01 for pure sulfates to 0.04 for fly ash, 0.2 for dust, and 0.77 for soot. Thus soot, even at 10% of the total fine particle mass, can enhance particle absorption by an order of magnitude. Soot was found in most samples as far south as 6°S (Figure 1). The ω values, obtained by several independent methods, are summarized in Plate 10 and are generally in the range between 0.85 to 0.9 for the near-surface values and between 0.8 to 0.9 above the surface layer, and about 0.86 to 0.9 for the column averages, in excellent agreement with the column average MACR value shown in Plate 10. Generally, these values represent a highly absorbing aerosol. The surface stations at Goa and Dharwad also determined column average SSA to be about 0.9 from optical measurements, the only data we have at the source [*Leon et al.*, this issue].

In view of the diverse sources and processes influencing the formation and evolution of continental aerosol, the narrow range (0.85 to 0.9) of the mean ω in Plate 10 is somewhat surprising. There are two plausible explanations. First, aerosol

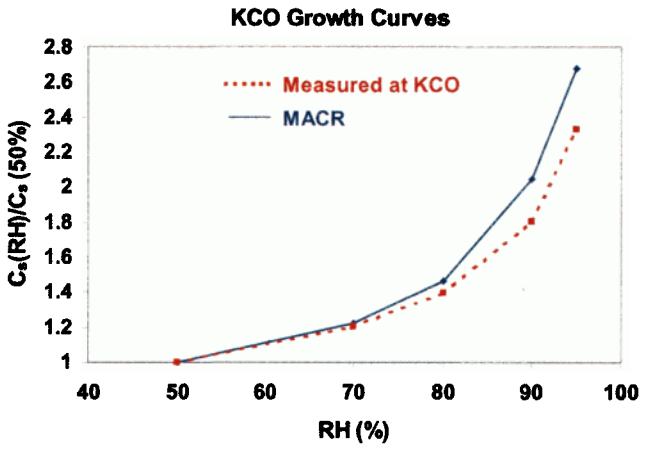

Plate 11. A comparison of the model-estimated growth curve with that observed at KCO. The growth curve is obtained by measuring scattering coefficient C_S as a function of relative humidity using two 3-wavelength nephelometers (one control at fixed relative humidity, the other at variable relative humidity; see *Ogren et al.* [1992] for details). Some investigations shows that the aerosols are occasionally coated with surface active materials that hinder their water uptake and thus influence their growth with relative humidity [*Ogren et al.*, 1992; *Cantrell et al.*, 1997]. This effect is not included in the present study. This could be one reason for the slight difference in the growth curves. This is also supported by the fact that measured growth rate is less than the modeled.

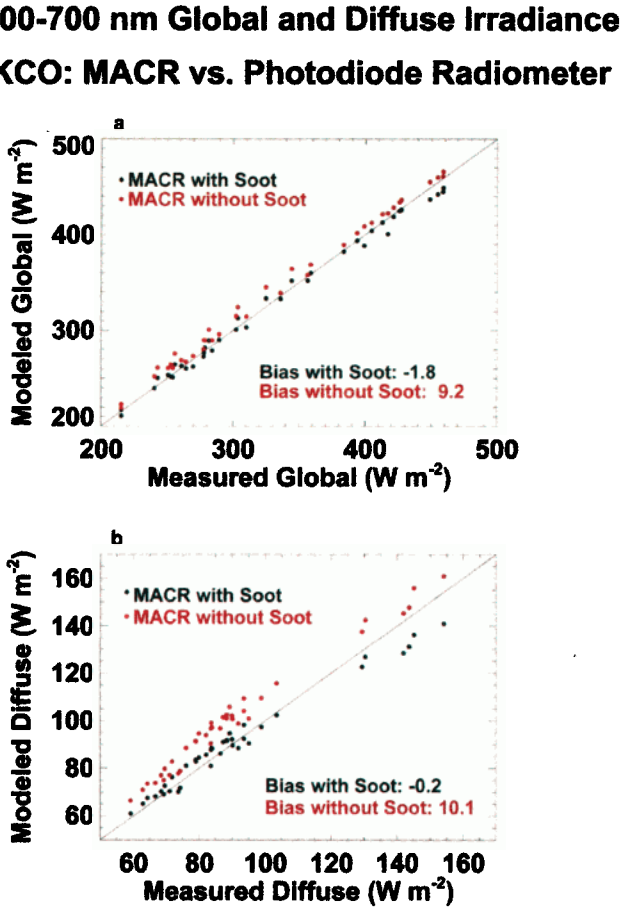

Plate 12. MACR predictions of clear-sky (a) global and (b) diffuse surface irradiance in the 0.4–0.7 μm photosynthetically active spectral band versus KCO measurements made by the BSI GTR-511c photodiode flux radiometer from February–March 1999. Details of the model, the measurement, and the angular, spectral, and absolute calibrations used to reduce the data are described by *Conant* [2000]. Black points represent the MACR model as described by S99. Red points represent MACR predictions when soot aerosol is removed from MACR (see Plate 8) and replaced with proportionate contributions from other aerosols so that τ_a remains constrained to the spectral observations. This plate demonstrates the importance of aerosol chemistry on the radiative fluxes.

combustion sources are widespread (as opposed to being localized over few urban centers) and rather similar. Second, the persistence of the monsoon flow often results in the mixing and dispersion of this aerosol over large regions with little modification. A more direct piece of evidence for the narrow range can be found in the C-130 data shown Plates 7a–7c. The data obtained from the cross-equatorial gradient flight of C-130 show the boundary layer concentration of the total aerosol condensation nuclei concentration ("cold CN") along with the so-called "hot CN" (the aerosol CN left after heating it to 300°C). The hot CN is indicative of refractory material (soot, fly ash, and sea salt). The ambient and heated size distribution of this aged NIO aerosol showed little change (other than concentration) so that the variations in CN (and hot CN) are reflected in the aerosol scattering (and the absorption). While CN and hot CN decrease with latitude significantly, their ratio is nearly constant. The near constant ratio suggests that the aerosol characteristics (e.g., ω) remain the same as the plume dilutes in time. The reason for this near constancy in the Northern Hemisphere hot CN/cold CN ratio is most likely that the black carbon aerosol component is first formed at high temperatures as primary particles upon which organics, sulfates, and other compounds later react or condense [*Clarke et al.*, 1998]. Evidence for this is shown in Plates 7b and 7c, in which the size distributions of the hot CN and the cold CN are shown for a case in the Southern Hemisphere (Plate 7b) and one in the Northern Hemisphere (Plate 7c). After the nonrefractory material (e.g., sulfates, nitrates, and most organic carbon) is evaporated from the aerosol, the remaining particles are equal in number, but far smaller in size. The shift to smaller sizes is far less prominent for the NH aerosol, indicating a large refractory component. Because the total particle count is within 5% for the heated and the unheated scans, it is concluded that essentially all NH aerosols have a primary, refractory component consisting of soot or perhaps fly ash that amounts to 10–20% of the aerosol mass. The much smaller size and negligible associated mass of the SH refractory component found here is presumed to reflect incomplete volatilization of the aerosol due possibly to pyrolysis of surface films, submicrometer sea salt, and/or other trace contaminants.

6. Success of the MACR Integration

The ultimate test of MACR is its ability to simulate the observations. It agrees with the observed spectral dependence of the aerosol optical depth (S99), the growth of the aerosol with humidity (Plate 11), the observed scattering and absorbing coefficients at the surface in KCO, and the column averaged ω (Plate 10). It simulates the broadband and spectral solar irradiance at the surface and the TOA under a variety of

aerosol conditions within a few percent [S99; *Podgorny et al.*, 2000; *Conant*, 2000]. At KCO, 12 independent radiometers covering the entire solar spectrum were deployed to validate MACR predictions for τ_a ranging from 0.05 to 0.9. Plate 12 shows a comparison of the observed and the modeled global (direct solar plus diffuse sky radiation) radiation (Plate 12a) and diffuse radiation (Plate 12b) for the 0.4 to 0.7 μm region. The agreement between the MACR and the observed values is well within the instrumental standard error of about 5 to 10 W m^{-2}. For the integrated 0.3 to 4 μm broadband irradiances measured by a pyranometer and a thermistor bolometer [*Valero et al.*, 1999], MACR agreed within 1–1.5% of the observed values. In addition, the modeled clear-sky TOA albedo values have been compared with the measured albedos by the Clouds and Earth's Radiant Energy System (CERES) [*Weilicki et al.*, 1996] radiation budget instrument on board the Tropical Rainfall Mapping Mission satellite. Again, the model agrees with the observed values to within 2% (S99).

Next, the radiances computed from MACR were used to develop an algorithm for retrieving τ_v from the NOAA advanced very high resolution radiometer (AVHRR) in the 0.63 μm spectral region. As shown by *Rajeev et al.* [2000] and *Rajeev and Ramanathan* [2001], the collocated τ_v between the retrieved and the measured values from Sun photometers at KCO and R/V *Sagar Kanya* agreed within the instrumental error of about ± 0.03. Lastly, the MACR values for the TOA and surface aerosol forcing agree with the observed values [*Satheesh and Ramanathan*, 2000, hereafter referred to as SR] within 10%.

7. Aerosol Direct Forcing in Cloudy Skies

In this section we consider the direct forcing due to all aerosols, including natural and anthropogenic. The term "cloudy skies" refers to average conditions with a mixture of clear and overcast portions of the sky. The starting point for the analyses is SR's clear-sky aerosol direct forcing efficiency, f ($= \Delta F/\Delta\tau_a$, the rate of change of forcing per unit increase in τ_a).

SR used simultaneous clear-sky solar irradiance observations at the surface and TOA and τ_a for the KCO location, and demonstrated that the TOA f is $f(T) \approx -25$ W m^{-2} and at the surface, $f(S) \approx -75$ W m^{-2}. The atmospheric forcing efficiency, $f(A) = f(T) - f(S)$, is positive, and thus aerosol solar absorption is the reason for $f(S)/f(T) > 1$. We checked the validity of SR's f values for the rest of the INDOEX region by correlating the satellite CERES radiation budget data with the observed τ_a shown in Plate 5 for the entire tropical Indian Ocean [*Rajeev and Ramanathan*, 2001]. For the entire tropical Indian Ocean, $f(T) \approx -22$ W m^{-2} (with a 1-σ spatial variation of 5 W m^{-2}) compared to SR's -25 W m^{-2}. About 50% of the difference is due to the larger domain of the satellite data, and the balance is due to revisions in CERES data since publication of SR's paper. For $f(S)$, C-130 radiometric data [*Valero et al.*, 1999] confirmed SR's value of -70 to -75 W m^{-2}. Reassured by this validation, we used SR's values for $f(S)$. We obtain clear-sky regional forcing as a function of latitude and longitude by multiplying the observed $f(T)$ [$= -22$ W m^{-2}], $f(S)$ [$= -72$ W m^{-2}], and $f(A)$ [$= 50$ W m^{-2}] with the τ_a shown in Plate 5.

For absorbing aerosols, it is well known [*Penner et al.*, 1992; *Haywood and Shine*, 1997; *Kaufman et al.*, 1998] that $f(T)$ can change sign from cooling (negative) under clear skies to a large net heating for overcast skies. This effect is important only for low clouds [*Kaufman et al.*, 1998] below 3 km for INDOEX aerosols since the bulk of the aerosol is below this level (Plate 9). Because of this dependence on the low cloud fraction, and since low clouds have significant spatial (Plate 2) and temporal variations, the direct forcing for cloudy skies has to be determined regionally as a function of latitude and longitude. This would not have been possible without the integrated INDOEX data set. We use the observed forcing for clear skies and estimate the direct forcing for cloud-covered regions with MACR and weight the two with observed clear and cloud fraction, respectively. For these estimates, MACR employed in situ data for cloud thickness (1 km) and vertical location (0.5 km for cloud base and 1.5 km for cloud top), and the results described in the next section for cloud optical depth and effective drop diameter. Because of the strong diurnal variation of low clouds, we adopt the geostationary METEOSAT satellite data to obtain cloud cover. The average NIO diurnal mean low cloud cover we retrieve is 29% (diurnal average cover), but the average cloud cover can be as low as 15% (depending on the threshold temperature we use to distinguish clear from cloudy pixels in the satellite radiances). Given the present limitations of the available satellite data (the 5 km resolution of the METEOSAT is one limitation; the AVHRR has 1 km resolution, but it does not have the diurnal sampling capability), it is difficult to determine the low cloud cover more accurately. This twofold (15–29%) uncertainty in the satellite-retrieved low cloud fraction is the largest source of error in the cloudy-sky forcing estimates.

We will begin with the regionally averaged aerosol (natural plus anthropogenic) direct radiative forcing, shown in Plate 13. The grid values of τ_a (Plate 5) and cloud fraction (Plate 2) are adopted to obtain the results presented here. The forcing is first estimated as a function of latitude and longitude (from the τ_a and cloud fraction shown in Plates 5 and 2, respectively) from which the regional averages shown in Plate 13 are obtained. We account for the significant diurnal variations in cloud cover but ignore its day-to-day variation. The regionally averaged northern Indian Ocean (0°N to 20°N) (NIO) values for the TOA forcing [$F(T)$] due to the direct effect is -7 ± 1 W m^{-2} (Plate 13a) for clear skies. For cloudy skies the TOA direct forcing ranges from -0 to -4 W m^{-2}, with a mean of -2 W m^{-2}. Inclusion of clouds introduces a net heating of about 5 W m^{-2} (difference between clear- and cloudy-sky forcing) largely because of the aerosol absorption of the reflected radiation from clouds. Roughly 50% of the ± 2 W m^{-2} estimated error in the cloudy-sky direct forcing is due to the uncertainty in cloud fraction; about 25% is due to the uncertainty in the vertical profile of aerosols, and the balance of 25% is due to the uncertainty in clear-sky forcing. The plate also shows the forcing for the surface [$F(S)$] and the atmosphere [$F(A)$]. In summary, the TOA, the atmosphere, and the surface forcing values are $F(T) = -2 \pm 2.0$ W m^{-2}; $F(A) = 18 \pm 3$ W m^{-2}; and $F(S) = -20 \pm 3$ W m^{-2}, respectively. The cloudy-sky surface direct forcing is a factor of 10 larger than the TOA forcing, as opposed to a factor of 3 for clear skies (SR). About 60% of the large atmospheric forcing $F(A)$ is due to soot, and the balance is due to fly ash, dust, and water vapor absorption of the radiation scattered by aerosols.

Aerosols also absorb and emit infrared radiation. Their importance for the INDOEX region has been estimated using a model similar to that presented by *Lubin et al.* [1996]. Their model was modified to include INDOEX aerosols and is used in this study. The NIO averaged TOA IR aerosol forcing for

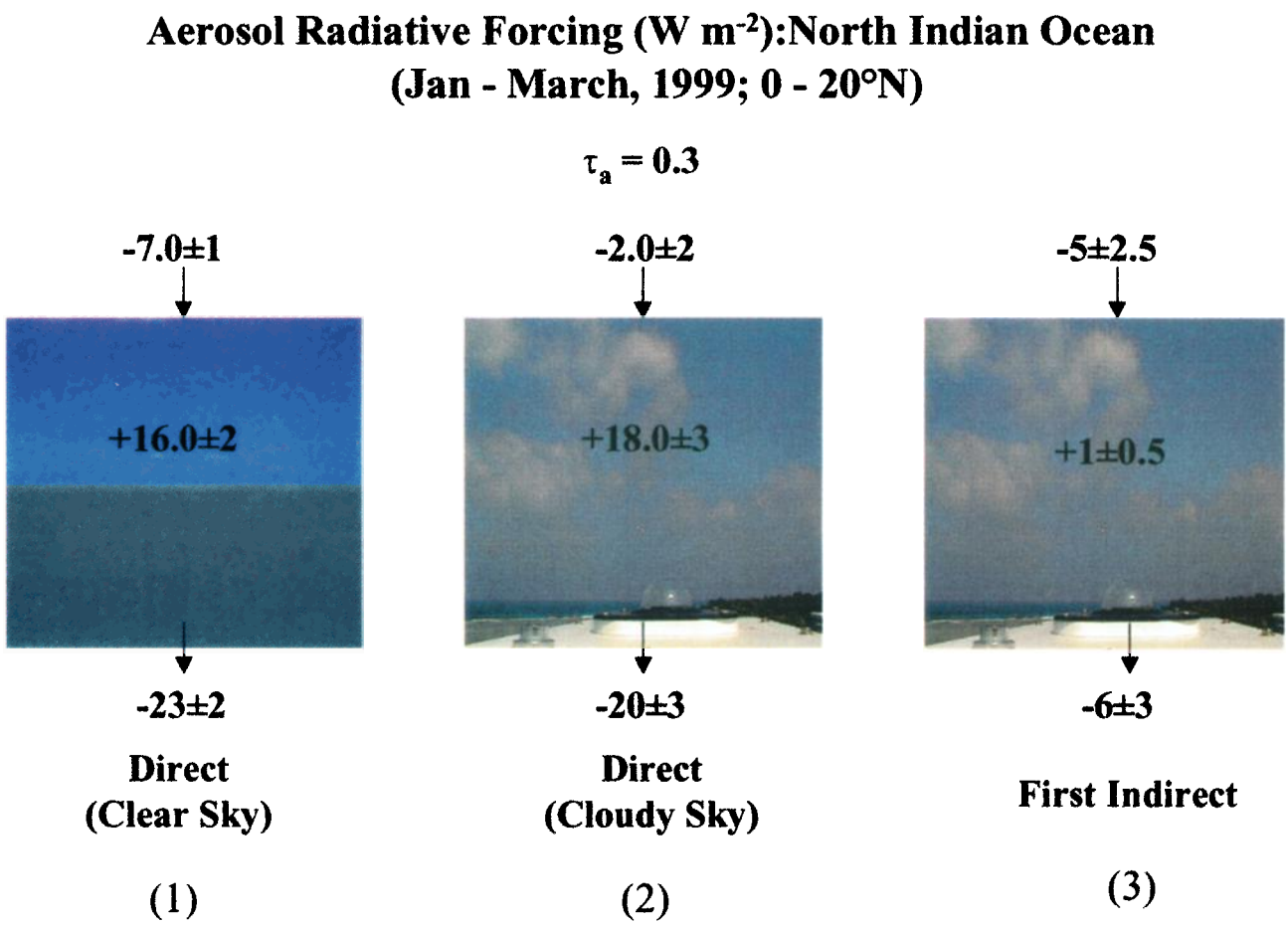

Plate 13. Aerosol direct radiative forcing for the North Indian Ocean (0° to 20°N; 40° to 100°E). The values include the effects of natural and anthropogenic aerosols. The values on top of each panel reflect TOA forcing; those within the box show the atmospheric forcing, and below the box is the surface forcing.

cloudy skies is 1.3 W m^{-2} at TOA and 5.3 W m^{-2} at the surface, such that the atmosphere is subject to a net cooling of −4.3 W m^{-2}. Thus they offset some of the solar forcing. Roughly 90% of the TOA IR forcing and 75% of the surface IR forcing are due to natural aerosols. The larger sea-salt and dust particles are more effective in their interaction with IR than the smaller anthropogenic particles.

8. Forcing Due to the First Indirect Effect

The C-130 data clearly demonstrated [*Heymsfield and McFarquhar*, this issue; *McFarquhar and Heymsfield*, this issue] that the polluted clouds have N_a (aerosol number density in particle sizes larger than 50 nm diameter) exceeding 1500 particles cm^{-3}, about the same average liquid water content, LWC ≈ 0.15 g m^{-3}, more cloud drops, $N_c \approx 315$ cm^{-3}, and smaller effective drop radii, $R_e \leq 6$ μm, compared with the pristine clouds {$N_a \leq 500$; $N_c = 90$ cm^{-3}; $R_e \geq 7.5$ μm}. The mean cloud base vertical velocity was about the same between the polluted and the pristine clouds, thus enabling the identification of the anthropogenic effect. The observed effect is captured in MACR through a composite scheme (described in detail in Appendix A) which relates the effective radius of cloud drops and the number density of cloud drops to N_a. Plates 14a and 14b compare this composite scheme with observed values. The three INDOEX points shown in Plates 14a and 14b are averages for the pristine ($N_a \leq 500$ cm^{-3}); the so-called transition ($500 \leq N_a \leq 1500$ cm^{-3}), and the polluted ($N_a \geq 1500$ cm^{-3}) cases. Each of these points is an average over 10,000 clouds sampled during 18 C-130 flights from 15°N to about 8°S. The horizontal bar shows the range of aerosol concentrations over which the data were averaged. The absolute accuracy of the cloud drop number density measurement is about 15%. The standard deviations of N_c in each of these ranges are large (as expected): 85 cm^{-3} for pristine; 135 cm^{-3} for transition, and 197 cm^{-3} for the polluted case. However, given the large number of clouds sampled, the standard error is expected to be much smaller than the above standard deviation. We estimate that the overall standard error in the averages shown in Plate 14 is about 25% or less [*Heymsfield and McFarquhar*, this issue; *McFarquhar and Heymsfield*, this issue]. The composite scheme is in agreement with the observed N_c. With respect to R_e, the observations seem to saturate around N_a of about 1500, whereas the predicted ones do not saturate until an N_a of about 2000. As a result, the predicted R_e for the larger N_a are smaller by about 10% (or 0.5 μm in radius). Plates 14c and 14d show the computed relationship between τ_a and N_a (Plate 14c) and between τ_c, the cloud optical depth at 0.5 μm, and τ_a (Plate 14d). We use this plate

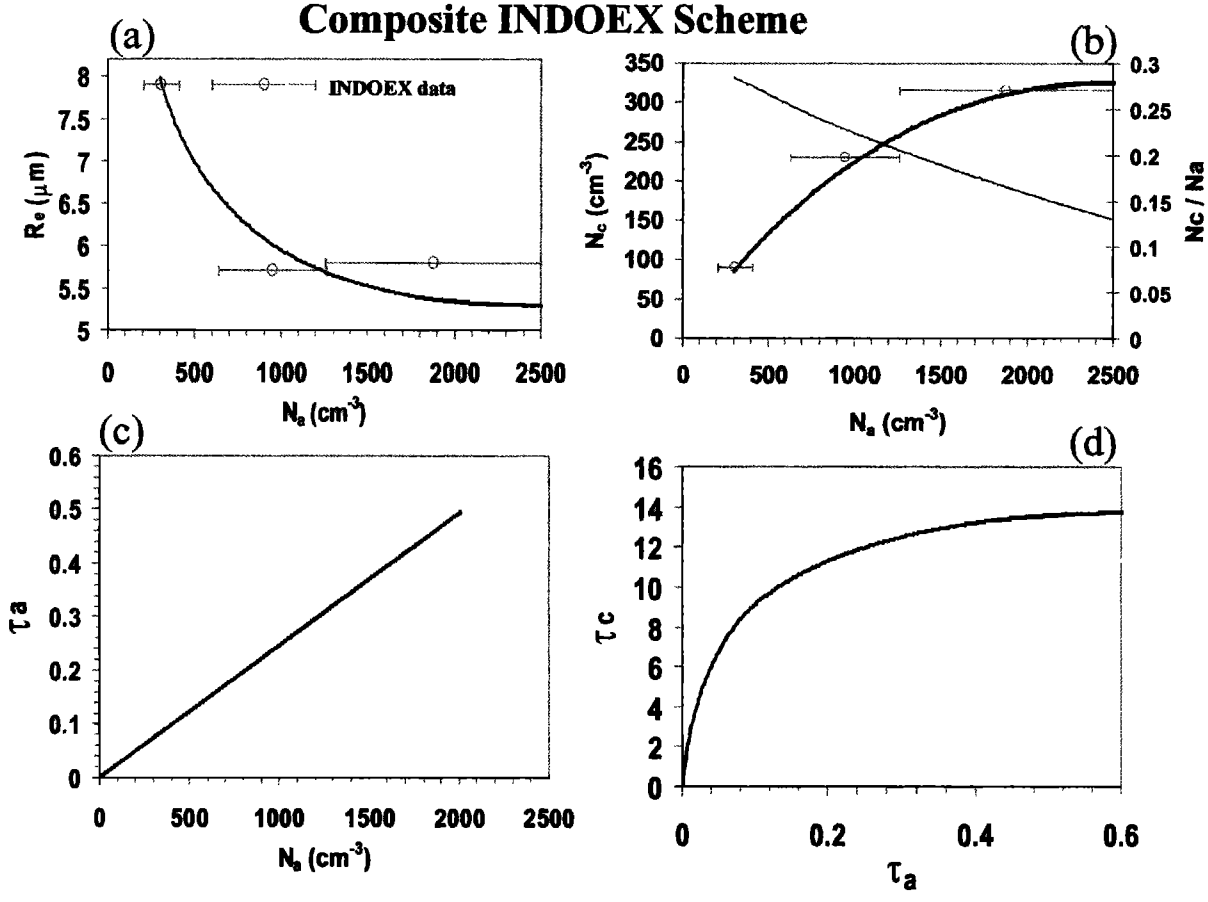

Plate 14. Comparison of the composite scheme with INDOEX in-cloud aircraft observations. (top left) Plot of R_e against N_a. In this and the other panels the horizontal bars are not error bars. Data have been binned within the N_a range shown by the horizontal bar, and averaged over several thousand points. (top right) Cloud drop number density N_c versus the aerosol number density N_a. (bottom left) Aerosol visible optical depth τ_a versus N_a. (bottom right) Cloud visible optical depth τ_c versus τ_a.

in conjunction with the regional distribution of τ_a (shown in Plate 5) to estimate the cloud optical depth for low clouds as a function of longitude and latitude. These values are employed in MACR to estimate the forcing due to the first indirect effect.

The first step is to estimate the N_a and τ_a for the NIO without any anthropogenic influence, i.e., the background natural aerosol over the tropical Indian ocean, subject to the continental outflow. If we adopt the result given in section 4 for the anthropogenic contribution of 80% to the column aerosol optical depth, we obtain the background τ_a to be 0.06 (20% of the 0.3 mean value for the NIO, shown in Plate 13). From Plate 14c this leads to a background N_a of about 300 cm^{-3}. This is slightly smaller than the measured N_a of about 350 cm^{-3} south of the ITCZ (Plate 7). We adopt τ_a of 0.07 and N_a of 350 cm^{-3} for the background unpolluted NIO value. Inserting these in MACR with the regional distribution of τ_a, τ_c, and cloud fraction (including the diurnal variation of clouds) on a 1° × 1° (latitude, longitude) grid, we obtain for the regional average forcing due to the first indirect effect: TOA equal to -5 ± 2 W m^{-2}; atmosphere equal to 1 ± 0.5 W m^{-2}; and surface equal to -6 ± 3 W m^{-2}. The large error bars are due mostly to the uncertainties in the satellite-retrieved cloud fraction. We first note that the TOA negative forcing due to the indirect effect is the same magnitude but opposite in sign to the positive forcing due to the direct effect of clouds; i.e., clouds on the one hand decrease the negative direct forcing by 5 W m^{-2} (from the clear-sky forcing of -7 to -2 W m^{-2} in cloudy skies), while on the other hand they enhance the negative forcing by -5 W m^{-2} through the first indirect effect. This important new result is largely because the absorbing aerosol layer is located within and above the tops of low clouds.

The latitudinal gradient of the sum of the direct and the first indirect forcing is shown in Plate 15. The aerosols introduce a large gradient in the solar heating, as shown in Plate 15. They exert a large positive 25 W m^{-2} north-south gradient in the solar heating of the atmosphere between 25°N and 25°S, and a correspondingly large negative gradient in the ocean solar heating.

We will conclude the discussion on forcing with a few comments on its year-to-year variability. The forcing numbers discussed thus far are valid for the year 1999 and that too for January, February, and March. Plate 4 suggests significant interannual variability in the optical depths. We should caution against an overinterpretation of this plate, for the cruise each year was not identical nor were the sampling dates. *Tahnk* [2001] uses 5-year AVHRR satellite data to obtain the following average τ_v (for January-February-March averages) for the northern Indian Ocean from 0°N to 30°N: 0.25 (1996); 0.29 (1997); 0.26 (1998); 0.27 (1999); and 0.25 (2000). Clearly, the NIO average forcing shown here is representative of the average forcing. However, the

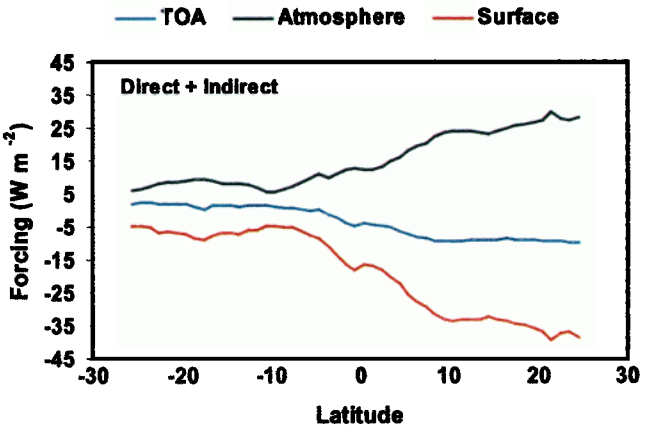

Plate 15. Latitudinal variation of the aerosol radiative forcing. Includes both natural and anthropogenic aerosols. The values have been averaged over ocean with respect to longitude from 40°E to 100°E.

variability depends on the spatial scale. For example, at KCO the 1999 values were higher than the 1998 and the 2000 τ_v values by about 40–50%. Thus the regional values shown here (e.g., Plate 15) may have significant interannual variability.

9. Second Indirect and Semidirect Effects

For the second indirect effect and the semidirect effect we rely on a three-dimensional eddy resolving trade cumulus model described by *Ackerman et al.* [2000]. Two independent model studies [*Ackerman et al.*, 2000; *Kiehl et al.*, 1999] of the INDOEX soot heating show that it leads to a reduction in the trade cumuli prevalent over the tropical oceans. *Ackerman et al.* [2000] insert the INDOEX aerosol with soot and estimate the forcing for various cloud drop concentrations (their Plate 5). We adopt here their simulations for N_c (cloud drop number density) of 90 cm^{-3} (pristine) and 315 cm^{-3} (polluted), consistent with the composite indirect effect scheme shown in

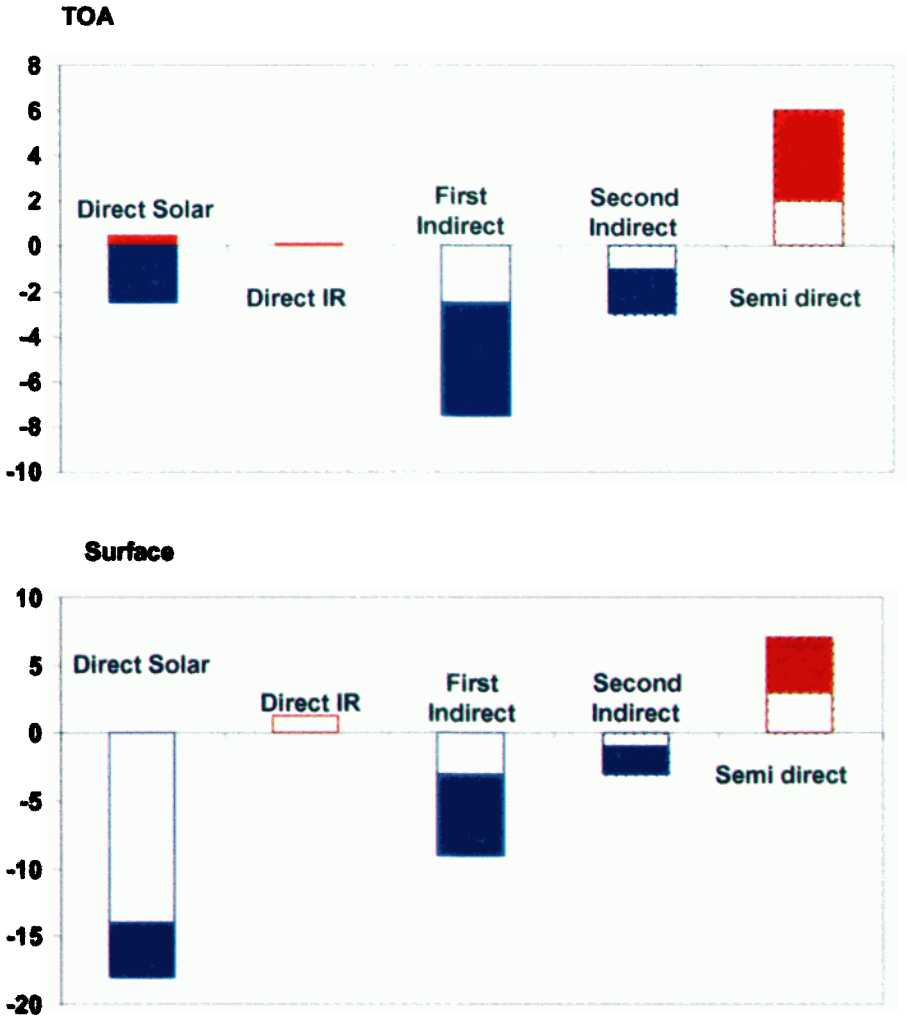

Plate 16. Regional average anthropogenic aerosol climate forcing for NIO (0° to 20°N; 40° to 100°E). The top panel shows the forcing at TOA, and the bottom panel shows it at the surface. The difference between the TOA and the surface forcing yields the atmospheric forcing. The uncertainty for each of the forcing values is the same as in Plate 13. The mean for the individual forcing terms should lie within the gray shaded region.

Plate 13. The inclusion of soot heating (semidirect effect) reduces the low cloud fraction by about 0.04 (day-night average). The TOA forcing due to this increase is about +4 W m^{-2} (day-night average). Their model also shows that addition of cloud drops (due to second indirect effect) enhances cloud lifetime, which in turn increases the low cloud fraction by about 2% and a forcing of −2 W m^{-2}. Given our poor knowledge of how the various uncertainties accumulate, we prefer not to attribute an overall uncertainty range to the total forcing (shown in the last column of Plate 16).

10. Anthropogenic Aerosol Forcing

As described earlier, the unpolluted τ_a is taken to be 0.07. In addition to the direct and the first indirect effect, we also include the second indirect effect and the semidirect effect. Lastly, we also include the IR forcing. The individual forcing values are shown in Plate 16. Furthermore, given the large uncertainty and the opposing signs of the various effects, we do not give a mean value, but instead show a gray shaded region that must contain the mean value. The clear-sky TOA forcing is −5 W m^{-2}, but the enhanced aerosol solar absorption in cloudy regions cancels out as much as 3 to 5 W m^{-2}. Thus the TOA direct effect (+0.5 to −2.5 W m^{-2}) is a small difference between two large numbers. The surface forcing, however, is as large as −14 to −18 W m^{-2}. The other terms shown in Plate 16 have been described earlier. In view of the large uncertainty in the satellite-retrieved low cloud cover and the competing nature of the various aerosol forcing terms, the total aerosol forcing is not shown in Plate 16. The regional distribution of the direct plus the first indirect forcing is shown in Plate 17. The solar heating of the eastern Arabian Sea and Bay of Bengal is reduced by as much as 20 to 30 W m^{-2} (about 15%). The TOA forcing peaks in the cloudy and polluted Bay of Bengal region, with values between −6 and −15 W m^{-2}.

11. Discussion: Climate and Environmental Effects

It is generally believed [*IPCC*, 1995] that the TOA forcing determines global average surface temperature change. This paradigm is appropriate for greenhouse gases and for primarily scattering aerosols such as sulfates. For the absorbing aerosols, however, since the surface and atmospheric forcing can be factors of 3 to 10 larger and of opposite signs, we need to carefully examine the effects (regionally first and then globally) with three-dimensional climate models. As we discuss next, the most important effect of these aerosols may be on the hydrological cycle and the atmospheric circulation.

The seasonal and NIO averaged surface forcing of −20 W m^{-2} is large compared with the downward heat fluxes into the ocean. It is about 15% of the naturally occurring wintertime solar heating of NIO [*Oberhuber*, 1988] and about the same magnitude as the net downward heat flux into the ocean of 30 to 50 W m^{-2}. Even if we make the extreme assumption that the aerosol forcing is zero during the other 9 months, the annual mean forcing of the aerosols is still about 4% of the total solar heating of the ocean and about 20% of the net heat flux into the NIO. In this context, it is intriguing that a recent study of world ocean surface temperatures [*Levitus et al.*, 2000] has shown that the NIO is one of the few regions without a decadal warming trend in the recent past, while the SIO, the Atlantic, and the Pacific were subject to a significant warming trend during the last 50 years. The surface forcing can also impact the hydrological cycle. Roughly 80% of the net radiative heating of the tropical oceans is balanced by evaporation [*Oberhuber*, 1988]. If 80% of the −20 W m^{-2} is balanced by reduced evaporation, it would constitute a 15% reduction in the wintertime evaporation of about 100 W m^{-2} or a 5% reduction in the annual mean evaporation. Ultimately, the decreased evaporation must lead to decreased tropical rainfall, thus perturbing the water budget. In addition, reduction in rainfall is equivalent to a reduction in the latent heat released to the middle and upper troposphere with implications for the lapse rate and the Hadley and Walker circulations.

We describe next another potentially new effect of aerosols on climate. The atmospheric forcing of about 15 W m^{-2} is equivalent to a heating rate of about 0.4 K/day for the 0 to 3 km layer and is about 50% of the climatological solar heating of this region. Furthermore, the heating rate increases from about less than 0.1 to 0.8 K/day over South Asia (Plate 18), forming a diabatic heating pattern asymmetric with respect to the equator and concentrated north of ITCZ. For comparison, the midtropospheric heating anomaly during El Niño events is nearly symmetric around the equator with its local maximum reaching up to 2.0 K/day south of the ITCZ [*Nigam et al.*, 2000]. What is the impact of the unique heating perturbation shown in Plate 18 on the atmospheric general circulation?

We made a preliminary assessment of such an impact with Version 3 of the Community Climate Model (CCM3) [*Kiehl et al.*, 1998]. Eighty-four years of the CCM3 "control run" were contrasted to 30 years of the model "experiments," each with the same prescribed climatological seasonal cycle of sea surface temperatures. In the experiment we applied the radiative heating increase in the levels below 700 mbar, which roughly correspond to the first 3 km above the surface. The surface solar flux is reduced with the ratio R, $F(S)/F(A)$, to be −1.5. This ratio approximates the clear-sky direct forcing at the surface (see Plate 13). The imposed heating varied temporally starting from zero in October; increased linearly to the peak value in March; and was restricted to NIO and the south Asian region with a smooth transition to zero outside this domain (Plate 19a) to prevent numerical "shocks." Plate 19 depicts the difference between the mean of control run and the mean of experiment both averaged for the months of January, February, March, and April. Plates 19b and 19c show the computed changes in temperatures and precipitation as an example of the nature and magnitude of the calculated changes.

The low-level air temperature T increases by about 0.5 to 1.5 K where the aerosol heating was imposed (Plate 19b). The warming also extended beyond the domain of the aerosol heating, in a southwest to northeast direction from the southern Indian Ocean to east Asia. However, the surface over South Asia cooled (not shown), but the magnitude was strongly dependent on the ratio R. For a ratio of 1.5, as in this plate (appropriate for clear skies), the surface cooled by as much as 1 K, while for a ratio of about 1.0 (similar to cloudy-sky values), the cooling was a factor of 2 to 3 smaller. The low-level heating enhances the rising motion locally. The dynamical response to this low-level heating is to enhance moist convection and strengthen the rainfall along the ITCZ (see the red shaded Indian Ocean region in Plate 19c) by as much as 15 to 30%. Since the rising air has to sink elsewhere, the subsidence increases away from the region of enhanced precipitation and leads to decreased rainfall north (in the Arabian Sea) and

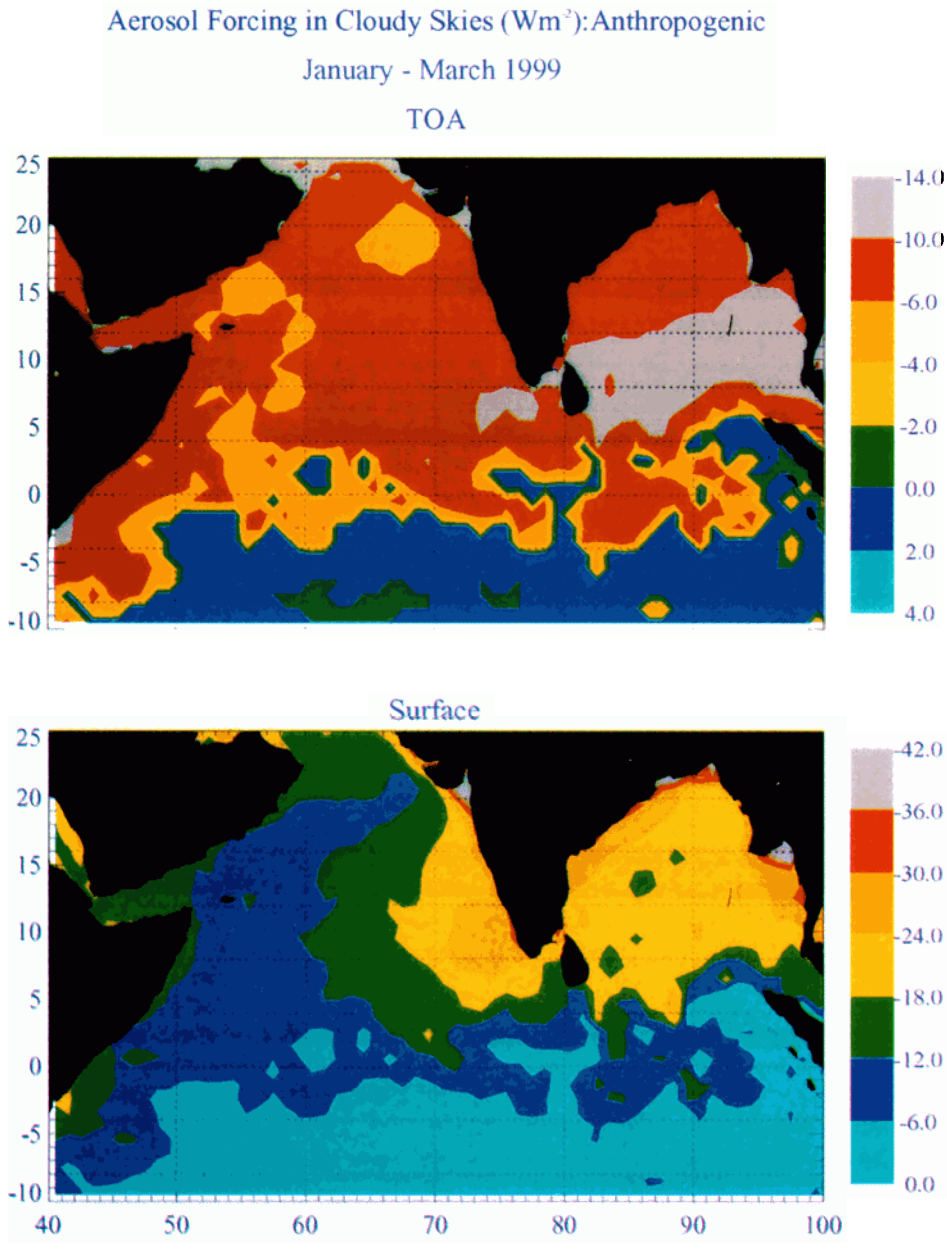

Plate 17. Regional distribution of the aerosol climate forcing for January–March 1999 at TOA (top panel) and at the surface (bottom panel).

south (over the western Indian Ocean) of the region of positive rainfall.

The enhanced ITCZ precipitation over the Indian Ocean also perturbs the east-west Walker circulation, which results in alternating patterns of suppressed rainfall over the western Pacific (see the negative rainfall regime over the tropical western Pacific) and enhanced rainfall over the eastern Pacific (not shown). This remote teleconnection between the west Pacific, the east Pacific, and the Indian Ocean rainfall is well known and well studied as part of the El Niño problem [*Rasmusson and Carpenter*, 1983]. Because of a decrease in the low-level wind, surface evaporation over the NIO decreased by 10 to 20 W m^{-2}, balancing more than 50% of the negative aerosol surface forcing (Plate 16b). These results have significant implications for global climate change and variability, particularly since absorbing aerosols are found in other regions of the world as well [see *Penner et al.*, 1992; *Kaufman et al.*, 1998].

In addition to perturbing the averaged forcing of the NIO, the aerosols perturb the interhemispheric heating gradients in the oceans in major ways. The climatological wintertime Indian Ocean solar heating varies from about 175 W m^{-2} north of 15°N to about 225 W m^{-2} south of 15°S [*Oberhuber*, 1988]. The 50 W m^{-2} latitudinal heating gradient should be compared with that of the surface aerosol forcing which varies from about -25 W m^{-2} north of 15°N to -2 W m^{-2} south of 10°S. This gradient, which (in addition to salinity gradients) is one of the driving forces for the thermohaline circulation, is enhanced by about 50%.

We should also consider the ecosystem impacts since 70% of the surface forcing is concentrated in the photosynthetically

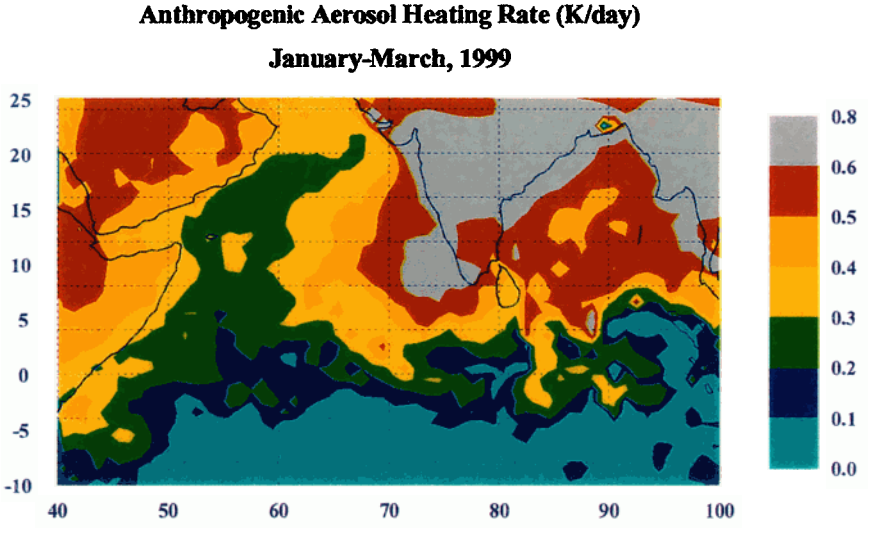

Plate 18. The 3-month (and diurnal) mean heating rate averaged between the surface and 3 km, due to anthropogenic aerosols. The ocean values were obtained from the integrated observations, while the land values were obtained from the 4-D assimilation model of *Collins et al.* [2001].

active UV and visible part of the solar spectrum [*Meywerk and Ramanathan*, 1999; *Conant*, 2000]. Since the percentage reduction in the UV and the visible region is as large as 10% to 20%, effects on terrestrial and marine biological productivity need to be examined. For example, *Chameides et al.* [1999] indicates that the haze-induced reduction of sunlight by about 10% can significantly reduce wheat and rice productivity in China. Increased aerosol concentration can also suppress precipitation from low clouds [*Albrecht*, 1989]. This effect together with the soot effect on burning low clouds [*Ackerman et al.*, 2000] can decrease significantly the wet removal of aerosols and potentially accelerate the increase in the thickness of the haze in the future.

The present findings can also have global implications. The large surface forcing and the atmospheric heating require absorbing aerosols with $\omega \leq 0.95$ and $\tau_a \geq 0.2$. Large surface forcing values similar to those shown here were found in the northern Atlantic off the East Coast of the United States [*Hignett et al.*, 1999]. Second, absorbing aerosols with ω of 0.9 are typical of aerosols resulting from biomass burning [*Kaufman et al.*, 1998]. As described by *Andreae and Crutzen* [1997], biomass burning was practiced in almost all the populated regions and is still practiced in many parts of the tropics and subtropics. Third, ice core data have revealed that soot concentrations have tripled between the 1850s to 1970s in western Europe [*Lavanchy et al.*, 1999], thus suggesting that absorbing aerosols such as those found in INDOEX were more prevalent in Europe and possibly North America at least until the 1970s. Lastly, electron microscopic images and particle analysis (Figure 1) show that the soot lodged in submicron sulfate and organic aerosols is transported as far south as 6°S, providing evidence that these particles survive in the atmosphere for more than a week, the transport time from South Asia to the ITCZ. Furthermore, peak concentrations of soot can extend up to 3 km (Plate 9; also see the soot layer extending to cloud tops in Plate 1). Forward trajectories (see a few samples of 7-day back trajectories in Plate 1) indicate that the air masses between 500 mbar (shown in Plate 1) and 700 mbar in the tropical Indian Ocean [*Krishnamurti et al.*, 1998] can travel within a week to as far away as mid-Pacific to North America. Thus the absorbing aerosols may extend far beyond the source regions.

The aerosol effects on climate can be large and complex involving many components of the global system. The INDOEX campaign has successfully demonstrated that an integrated observing system that combines in situ determination of the physico-chemical properties at the particles scale up to the synoptic scale with satellite measurements of the entire ocean basin and models of the chemical-physical-dynamical system can answer fundamental questions such as, What is the impact of developing nations in South Asia on regional and global radiation balance and climate? Advances in observing systems, information technology, modeling, and collaboration across disciplinary and national boundaries were the recipes that contributed to this success.

Appendix A: The Composite First Indirect Effect Scheme Adopted in MACR

The aerosol indirect effect is difficult to quantify as it depends on the interactions between aerosols, CCN, and cloud properties which are poorly understood [*Jones et al.*, 1994; *Heintzenberg et al.*, 1997]. Many attempts have been made since the 1990s to tackle this problem [*Jones et al.*, 1994; *Meehl et al.*, 1996; *Jones and Slingo*, 1996; *Kogan et al.*, 1996; *Chuang et al.*, 1997; *Le Treut et al.*, 1998; *Han et al.*, 1998; *Brenguier et al.*, 2000]. For our composite scheme we adopt a more detailed approach to estimate the anthropogenic indirect aerosol forcing from combined surface, aircraft, and satellite observations.

Two fundamental relationships characterize the indirect effect: the dependence of N_c on N_a; and the dependence of effective radii R_e on N_a. These parameters in turn depend on the vertical velocity W, the cloud liquid water content L, and the chemical composition of aerosol concentration (which influences the CCN activation spectra). The vertical velocity and the CCN supersaturation spectrum regulate the supersaturation S, which determines the number of activated CCN; in addition, W plays some role in determining L. Entrainment

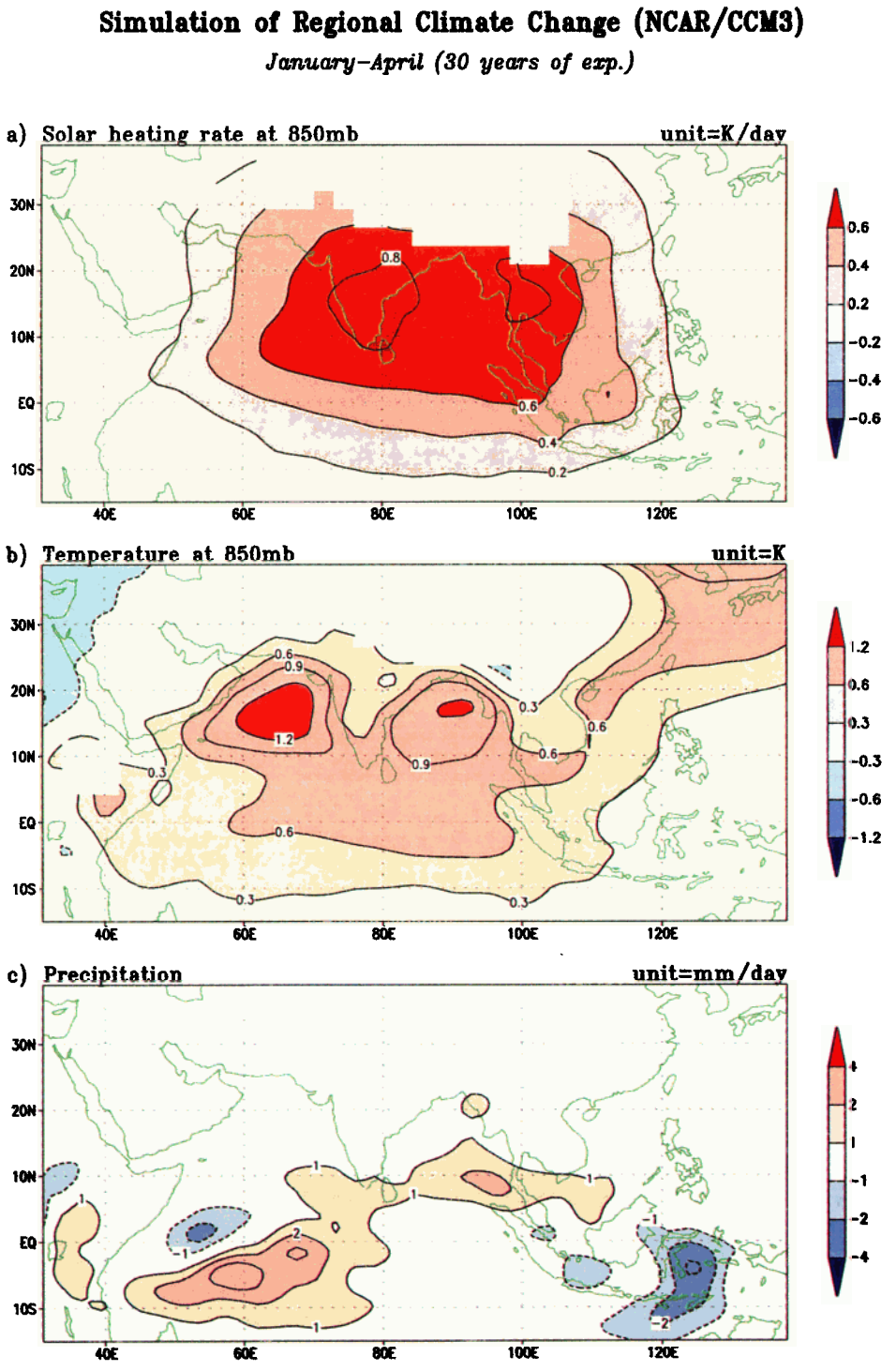

Plate 19. Difference (experiment − control run): (a) short-wave radiative heating at 850 mbar, (b) air temperature at 850 mbar, and (c) precipitation. The "control run" was generated from NCAR/CCM3 (atmospheric model) with the interactive land surface model and with the climatological seasonal cycle of observed SSTs. The January–April average is taken here of the difference between 30 years of experiment and 84 years of control run. In the experiment, INDOEX aerosol climate forcing of "best-guessed" ideal pattern was applied to the period between October and May. This additional forcing consists of low-level atmospheric heating and surface solar-flux reduction, in which the ratio R, $F(S)/F(A)$, is about -1.5. In another experiment (not shown) where $R \sim -1.0$, air temperature change at 850 mbar is somewhat less, but the precipitation change remains largely unchanged.

and cloud thickness, two macroscopic parameters of cloud dynamics, also govern L. As shown by *Heymsfield and McFarquhar* [this issue] and *McFarquhar and Heymsfield* [this issue] (hereafter referred to as HM and MH, respectively), the mean and median W, L, and cloud width Δx, while undergoing significant cloud-to-cloud variability, was about the same between the northern and southern tropical Indian Ocean and between polluted and pristine conditions. HM and MH use the long transequatorial gradient flights to bin the aircraft data as follows: pristine, $N_a \leq 500$ (cm^{-3}); polluted, $N_a \geq 1500$ cm^{-3}; and transition region, 500 $cm^{-3} < N_a < 1500$ cm^{-3}. For all these three regimes the median values were $W \approx 0.4$ m s^{-1}; $L \approx 0.15$ g m^{-3}; and $\Delta x \approx 300$ m. This remarkable similarity enabled MH and HM to discern the indirect effect from the data and parameterize it.

Numerous attempts [*Taylor and McHaffie*, 1994; *Martin et al.*, 1994; *Snider and Berenguier*, 2000] have been made to characterize the indirect effect from aircraft data collected over the Atlantic (mostly) and the eastern Pacific. Our scheme is based on the conclusions of these earlier aircraft studies: First is the *Martin et al.* [1994] study which includes a comprehensive set of data from the British meteorological services C-130 data from the eastern Pacific, the South Atlantic, the subtropical Atlantic, and the British Isles. These data reveal that N_c and N_a are correlated in a statistically significant manner. Second is the *Snider and Berenguier* [2000] ACE 2 study, which concludes that *Twomey*'s [1977] theoretical expressions relating droplet concentrations based on updraft velocity and the CCN activation spectrum are consistent with direct observations. Next is the finding of several studies [e.g., *Martin et al.*, 1994; *Taylor and McHaffie*, 1994; MH] that the effective cloud drop radius is related to L and N_a in a predictable manner. We follow the approach proposed in these studies, which is to relate R_e in terms of L and N_c [e.g., see *Martin et al.*, 1994, equation (11)] and to relate N_c in terms of N_a, the supersaturation S, and the vertical velocity W. The composite INDOEX scheme described here adopts the MH parameterization for R_e and a combination of CCN spectra measured at KCO and aircraft data for N_a, L, and ΔZ (cloud thickness). The resulting scheme is tested against the binned data presented by HM and then compared with data from other field studies.

The scheme accounts for the following measurements: (1) CCN spectra measured at KCO from 0.1 to 1%; (2) the dependence of the supersaturation on aerosol concentration as measured from aircraft; (3) the microphysical data reported by HM for pristine and heavily and moderately polluted conditions; and (4) the dependence of effective radii on cloud drop number concentration as reported by MH.

Unless otherwise stated, all of the values and functional relationships described below are valid only in the following range:

$$300 \text{ cm}^{-3} \leq N_a \leq 2000 \text{ cm}^{-3}.$$

At KCO, cloud condensation nuclei (CCN) at different applied water vapor supersaturations (0.1 to 1%) were measured along with simultaneous determinations of the aerosol size distributions in the particle diameter range from 10 to 500 nm [*Cantrell et al.*, 2000, this issue]. The cloud condensation nuclei measurements were made with a cloud condensation nucleus counter, while the aerosol size spectrum was derived with a scanning mobility particle sizer as described by *Ji et al.* [1998]. The CCN spectra [*Cantrell et al.*, 2000, this issue] which fits the power law assumed in most studies [e.g., *Twomey*, 1977; *Snider and Brenguier*, 2000; HM] is

$$\text{CCN} = CS^k \qquad k = 0.76. \tag{A1}$$

The parameter S is the water vapor supersaturation in percent, and the parameter C, by definition, is the CCN for $S = 1\%$ which increases with the aerosol concentration as N_a^n, with $n = 1.16$ yielding the best fit. The value of $k = 0.76$ is in excellent agreement with the average value of 0.8 reported for ACE 2 by *Snider and Brenguier* [2000]. Upon combining this dependence of C (CCN at $S = 1\%$) on N_a with (A1), we obtain a power law relationship: $\text{CCN} = bN_a^nS^k$, where b is a constant. However, when we fit this equation with the KCO CCN data, we find that $n = 1.25$ gives the best fit for $S < 0.5\%$ and $n = 1.16$ for $S \geq 0.5\%$. This empirical dependence of n on S may be simply due to the measurement uncertainty in CCN (about 40%), N_a (about 20%), and S (not quantified yet) or poorly understood microphysical processes. Since the effective in-cloud S is less than or equal to 0.3%, we adopt the following equation:

$$\text{CCN} = 0.12N_a^{1.25}[S/0.3]^{0.76} \qquad \text{for } S \leq 0.3\%$$
$$\text{and } 300 \leq N_a \leq 2000 \text{ cm}^{-3}. \tag{A2}$$

Plate A1 compares the CCN predicted by (A2) with *Cantrell et al.*'s [2000, this issue] observed CCN for $S = 0.5\%$ from R/V *Ron Brown* (for the entire cruise shown in Plate 2a) along with KCO data. Equation (A2) is shown for both $n = 1.16$ and 1.25, and the two curves capture the observed CCN. We show both values of n, since $n \approx 1.16$ for $S = 1\%$ and is about 1.25 for $S \leq 0.3\%$, with a value somewhere in between for $S = 0.5\%$. Since we use in situ data, the equation accounts for the possibility of some fraction of the aerosol being hydrophobic depending on the fraction of anthropogenic and natural aerosols. Modeling of the cloud activation process using the supersaturation spectra from KCO or (A2) indicates that cloud droplet concentrations should be significantly elevated over "clean region" clouds, as indeed was found to be the case from measurements made aboard the NCAR C-130.

The effective supersaturation that explains the observed (averaged) N_c [*Hudson and Yum*, 1997, 1999] is 0.1–0.2% for the pristine case ($N_a \leq 500$) and about 0.05% for the most polluted case ($N_a > 1500$). Entrainment, which plays an important role in limiting N_c, does not enter explicitly in our scheme, but is implicitly factored into the inferred value of effective supersaturation. The inverse correlation between S and N_a is predicted by *Twomey*'s [1977] theory (the equation is given later in this section) and has also been observed by other field studies (see summary in the work of *Finlayson-Pitts and Pitts* [2000]). It arises from the fact that as more drops are nucleated, the vapor supply is depleted, and as a result, S is reduced. In order to account for this, we let S vary with N_a as follows:

$$S = 0.18 \exp(-6.5 \times 10^{-4}N_a) \qquad 300 \leq N_a \leq 2000. \tag{A3}$$

Thus, given N_a, we can estimate the CCN from (A2) and (A3). Only a fraction f of the CCN become cloud drops. We adopt the aircraft data reported by *McFarquhar and Heymsfield* [this issue] and by *Hudson and Yum* [1997, 1999], which indicate that $f = 1$ for pristine conditions ($N_a \leq 300$) and for larger values of N_a the observed N_c was about 0.8 of CCN. The following equation accounts for this behavior:

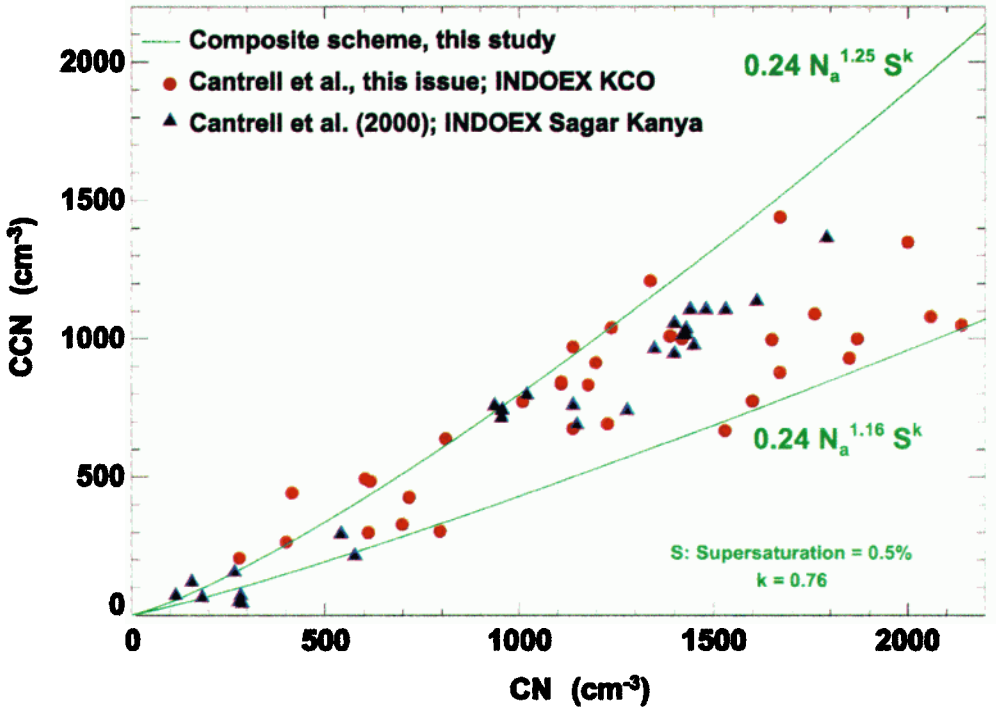

Plate A1. Variation of cloud condensation nuclei (CCN at 0.5% supersaturation) with condensation nuclei (CN) (N_a in the text). Comparison of observations (at KCO and over the tropical Indian Ocean) with the composite scheme. The precision of the CCN measurements is about ±20%.

$$N_c = f \times \text{CCN} \qquad f = 0.8 + 0.2 \cdot \exp\{(N_a - 300) \times 0.004\} \qquad N_a \geq 300. \tag{A4}$$

The next parameter we need is the effective radius R_e, defined as follows:

$$R_e = \frac{\int R^3 n(R)\, dR}{\int R^2 n(R)\, dR}. \tag{A5}$$

We use the parameterization developed by MH, who in turn follow *Martin et al.* [1994] for obtaining R_e from aircraft data. Martin et al. express R_e in terms of L and N_c:

$$R_e = \left\{\frac{3L}{4\pi K N_c}\right\}^{1/3}, \tag{A6}$$

where MH obtain the following K values from INDOEX data: $K = 0.83$ for pristine clouds ($N_a \leq 500$); and $K = 0.73$ for heavily polluted clouds ($N_a \geq 1500$). The factor K accounts for the deviation from monodisperse (all drops having the same radius) size distributions. It can easily be shown from (A5) or (A6) that $K = 1$ for monodispersed distributions. With estimates for N_c, R_e, and N_a we can calculate, using MACR, the cloud optical depth and radiative forcing, provided we know L, cloud base altitude Z_b, and cloud thickness ΔZ. Following HM, we adopt $L = 0.15$ g m^{-2}; $Z_b = 600$ m; and $\Delta Z = 300$ m. The N_a values at cloud base are used for (A2) and (A4). Using the vertical distribution of aerosols shown in Plate 9, the relationships between the various parameters as obtained by MACR are shown in Plate 14. Typically, two types of aerosol vertical distributions were observed (Plates 9a and 9b): one in which the aerosol layer is concentrated in the boundary layer (Plate 9a) and another in which an elevated layer is observed near 3 km (Plate 9b). The elevated aerosol vertical structure was also observed over India (from an INDOEX lidar in Goa) containing half or more of the total aerosol extinction. Because of uncertainties in the actual data, we do not use the actual values in Plate 9, but normalize the value at each altitude with τ_a (obtained from vertically integrating the profile) and then multiply it with the τ_a from Plate 5. We include both the profiles shown in Plates 9a and 9b, weighting our forcing estimates with the frequency of occurrence, 2/3 for the elevated layer aerosol profile and 1/3 for the boundary layer aerosol profile.

The cloud fractions are retrieved from METEOSAT data (IR brightness temperature). In general, the atmospheric conditions are classified into eight as follows: clear sky; clear sky with cirrus; broken low clouds; broken low clouds with cirrus; low clouds; low clouds with cirrus; anvils; and deep cumulus. The eight categories are subgrouped into three: clear sky; total low clouds; and high clouds. We used three types of sky conditions, specifically, clear skies, low clouds (including cirrus), and convective clouds including anvils.

Acknowledgments. INDOEX was funded by numerous national agencies including the National Science Foundation (lead agency for the U.S. program), the Department of Energy, NASA, NOAA, Indian Space Research Organization, European Union for Meteorological Satellites (EUMETSAT), Max Planck Institute, French Centre National d'Etudes Spatiales (CNES), and Centre National de la Recherche Scientifique (CNRS). Seed funds for INDOEX were provided by

the Vetlesen foundation and the Alderson foundation. We thank EUMETSAT for moving METEOSAT to the Indian Ocean; the Government of Maldives for hosting INDOEX; J. Fein for his keen interest and support for INDOEX; E. Frieman and C. Kennel for their enthusiastic support; the University Corporation for Atmospheric Research for conducting the field operations; and the crew of the aircraft and the ships. We thank M. Lawrence, J. Williams, and the two *JGR* referees for their comments on an earlier draft.

References

Ackerman, A. S., O. B. Toon, D. E. Stevens, A. J. Heymsfield, V. Ramanathan, and E. J. Welton, Reduction of tropical cloudiness by soot, *Science*, *288*, 1042–1047, 2000.

Albrecht, B. A., Aerosols, cloud microphysics, and fractional cloudiness, *Science*, *245*, 1227–1230, 1989.

Althausen, D., D. Müller, A. Ansmann, U. Wandinger, H. Hube, E. Clauder, and S. Zörner, Scanning 6-wavelength 11-channel aerosol lidar, *J. Atmos. Oceanic Technol.*, *17*, 1469–1482, 2000.

Andreae, M. O., and P. J. Crutzen, Atmospheric aerosols: Biogeochemical sources and role in atmospheric chemistry, *Science*, *276*, 1052–1058, 1997.

Bates, T. S., B. J. Huebert, J. L. Gras, F. B. Griffiths, and P. A. Durkee, International Global Atmospheric Chemistry (IGAC) Project's First Aerosol Characterization Experiment (ACE 1): Overview, *J. Geophys. Res.*, *103*, 16,297–16,318, 1998.

Brenguier, J. L., P. Y. Chuang, Y. Fouquart, D. W. Johnson, F. Parol, H. Pawlowska, J. Pelon, L. Schuller, F. Schroder, and J. Snider, An overview of the ACE-2 CLOUDYCOLUMN closure experiment, *Tellus*, *Ser. B*, *52*, 815–827, 2000.

Cantrell, W., G. Shaw, R. Benner, and D. Veazey, Evidence for sulfuric acid coated particles in the Arctic air mass, *Geophys. Res. Lett.*, *24*, 3005–3008, 1997.

Cantrell, W., G. Shaw, C. Leck, L. Granet, and H. Cachier, Relationships between cloud condensation nuclei spectra and aerosol particles on a south-north transect of the Indian Ocean, *J. Geophys. Res.*, *105*, 15,313–15,320, 2000.

Cantrell, W., G. Shaw, G. Cass, and K. Prather, Closure between aerosol particles and cloud condensation nuclei at Kaashidhoo Climate Observatory, *J. Geophys. Res.*, this issue.

Chameides, W. L., et al., Case study of the effects of atmospheric aerosols and regional haze on agriculture: An opportunity to enhance crop yields in China through emission controls?, *Proc. Natl. Acad. Sci.*, *96*, 13,626–13,633, 1999.

Charlson, R. J., J. Langner, H. Rodhe, C. B. Leovy, and S. G. Warren, Perturbation of the Northern Hemisphere radiative balance by backscattering from anthropogenic sulfate aerosols, *Tellus*, *Ser. A*, *43*, 152–163, 1991.

Charlson, R. J., S. E. Schwartz, J. M. Hales, R. D. Cess, J. A. Coakley, J. E. Hansen, and D. J. Hoffmann, Climate forcing by anthropogenic aerosols, *Science*, *255*, 423–430, 1992.

Chowdhury, Z., L. S. Hughes, L. G. Salman, and G. R. Cass, Atmospheric particle size and composition measurements to support light extinction calculations over the Indian Ocean, *J. Geophys. Res.*, this issue.

Christoforou, C. S., L. G. Salmon, M. P. Hannigan, P. A. Solomon, and G. R. Cass, Trends in fine particle concentration and chemical composition in Southern California, *J. Air Waste Manage. Assoc.*, *50*, 43–53, 2000.

Chuang, C. C., J. E. Penner, K. E. Taylor, A. S. Grossman, and J. J. Walton, An assessment of the radiative effects of anthropogenic sulfate, *J. Geophys. Res.*, *102*, 3761–3778, 1997.

Chylek, P., and J. Wong, Effect of absorbing aerosols on global radiation budget, *Geophys. Res. Lett.*, *22*, 929–931, 1995.

Clarke, A. D., and R. J. Charlson, Radiative properties of the background aerosol: Absorption component of extinction, *Science*, *229*, 263–265, 1985.

Clarke, A. D., et al., Particle nucleation in the tropical boundary layer and its coupling to marine sulfur sources, *Science*, *282*, 89–92, 1998.

Coakley, J. A., and R. D. Cess, Response of the NCAR Community Climate Model to the radiative forcing by the naturally-occurring tropospheric aerosol, *J. Atmos. Sci.*, *42*, 1677–1692, 1985.

Coffee, K. R., S. A. Guazzotti, and K. A. Prather, Variations in single particle chemical complexity of the marine aerosol during the Indian Ocean Experiment (abstract), *Eos Trans. AGU*, *80*(46), Fall Meet. Suppl., 183, 1999.

Collins, W. D., P. J. Rasch, B. E. Eaton, B. Khattatov, J.-F. Lamarque, and C. S. Zender, Simulating aerosols using a chemical transport model with assimilation of satellite aerosol retrievals: Methodology for INDOEX, *J. Geophys. Res.*, *106*, 7313–7336, 2001.

Conant, W. C., An observational approach for determining aerosol surface radiative forcing: Results from the first field phase of INDOEX, *J. Geophys. Res.*, *105*, 15,347–15,360, 2000.

Cooke, W. F., C. Liousse, H. Cachier, and J. Feichter, Construction of a 1° × 1° degree fossil fuel emission data set for carbonaceous aerosol and implementation and radiative impact in the ECHAM4 model, *J. Geophys. Res.*, *104*, 22,137–22,162, 1999.

Finlayson-Pitts, B. J., and J. N. Pitts Jr., *Chemistry of the Upper and Lower Atmosphere: Theory, Experiments, and Applications*, 969 pp., Academic, San Diego, Calif., 2000.

Grassl, H., Albedo reduction and radiative heating of clouds by absorbing aerosol particles, *Contrib. Atmos. Phys.*, *48*, 199–210, 1975.

Han, Q. Y., W. B. Rossow, J. Chou, and R. M. Welch, Global survey of the relationships of cloud albedo and liquid water path with droplet size using ISCCP, *J. Clim.*, *11*, 1516–1528, 1998.

Hansen, J., M. Sato, and R. Ruedy, Radiative forcing and climate response, *J. Geophys. Res.*, *102*, 6831–6864, 1997.

Haywood, J. M., and V. Ramaswamy, Global sensitivity studies of the direct radiative forcing due to anthropogenic sulfate and black carbon aerosols, *J. Geophys. Res.*, *103*, 6043–6058, 1998.

Haywood, J. M., and K. P. Shine, Multi-spectral calculations of the direct radiative forcing of tropospheric sulphate and soot aerosols using a column model, *Q. J. R. Meteorol. Soc.*, *123*, 1907–1930, 1997.

Hegg, D. A., R. J. Ferek, and P. V. Hobbs, Light scattering and cloud condensation nucleus activity of sulfate aerosol measured over the northeast Atlantic Ocean, *J. Geophys. Res.*, *98*, 14,887–14,894, 1993.

Heintzenberg, J., R. J. Charlson, A. D. Clarke, C. Liousse, V. Ramaswamy, K. P. Shine, M. Wendisch, and G. Helas, Measurements and modeling of aerosol single-scattering albedo: Progress, problems and prospects, *Contrib. Atmos. Phys.*, *70*, 249–263, 1997.

Heymsfield, A. J., and G. M. McFarquhar, Microphysics of INDOEX clean and polluted trade cumulus clouds, *J. Geophys. Res.*, this issue.

Hignett, P., J. P. Taylor, P. N. Francis, and M. D. Glew, Comparison of observed and modeled direct aerosol forcing during TARFOX, *J. Geophys. Res.*, *104*, 2279–2287, 1999.

Hobbs, P. V., An overview of the University of Washington airborne measurements and results from the Tropospheric Aerosol Radiative Forcing Observational Experiment (TARFOX), *J. Geophys. Res.*, *104*, 2233–2238, 1999.

Hobbs, P. V., J. S. Reid, R. A. Kotchenruther, R. J. Ferek, and R. Weiss, Direct radiative forcing by smoke from biomass burning, *Science*, *275*, 1776–1778, 1997.

Hudson, J. G., and S. S. Yum, Droplet spectral broadening in marine stratus, *J. Atmos. Sci.*, *54*, 2642–2654, 1997.

Hudson, J. G., and S. S. Yum, Droplet spectral broadening in marine stratus—Reply, *J. Atmos. Sci.*, *56*, 2264–2265, 1999.

Intergovernmental Panel on Climate Change (IPCC), *Climate Change 1994: Radiative Forcing of Climate, Report to IPCC From the Scientific Assessment Group (WGI)*, Cambridge Univ. Press, New York, 1995.

Jayaraman, A., D. Lubin, S. Ramachandran, V. Ramanathan, E. Woodbridge, W. D. Collins, and K. S. Zalpuri, Direct observations of aerosol radiative forcing over the tropical Indian Ocean during the January–February 1996 pre-INDOEX cruise, *J. Geophys. Res.*, *103*, 13,827–13,836, 1998.

Ji, Q., G. E. Shaw, and W. Cantrell, A new instrument for measuring cloud condensation nuclei: Cloud condensation nucleus "remover," *J. Geophys. Res.*, *103*, 28,013–28,019, 1998.

Jones, A., and A. Slingo, Predicting cloud-droplet effective radius and indirect sulphate aerosol forcing using a general circulation model, *Q. J. R. Meteorol. Soc.*, *122*, 1573–1595, 1996.

Jones, A., D. L. Roberts, and A. Slingo, A climate model study of indirect radiative forcing by anthropogenic sulphate aerosols, *Nature*, *370*, 450–453, 1994.

Kaufman, Y. J., and R. S. Fraser, The effect of smoke particles on clouds and climate forcing, *Science*, *277*, 1636–1639, 1997.

Kaufman, Y. J., et al., Smoke, Clouds, and Radiation-Brazil (SCAR-B) experiment, *J. Geophys. Res.*, *103*, 31,783–31,808, 1998.

Kiehl, J. T., and B. P. Briegleb, The relative roles of sulfate aerosols and greenhouse gases in climate forcing, *Science*, *260*, 311–314, 1993.

Kiehl, J. T., J. J. Hack, G. B. Bonan, B. A. Boville, D. L. Williamson,

and P. J. Rasch, The National Center for Atmospheric Research Community Climate Model: CCM3, *J. Clim.*, *11*, 1131–1149, 1998.

Kiehl, J. T., V. Ramanathan, J. J. Hack, A. Huffman, and K. Swett, The role of aerosol absorption in determining the atmospheric thermodynamic state during INDOEX (abstract), *Eos Trans. AGU*, *80*(46), Fall Meet. Suppl., 184, 1999.

Kiehl, J. T., T. L. Schneider, P. J. Rasch, M. C. Barth, and J. Wong, Radiative forcing due to sulfate aerosols from simulations with the National Center for Atmospheric Research Community Climate Model, Version 3, *J. Geophys. Res.*, *105*, 1441–1457, 2000.

Kleeman, M. J., G. R. Cass, and A. Eldering, Modeling the airborne particle complex as a source-oriented external mixture, *J. Geophys. Res.*, *102*, 21,355–21,372, 1997.

Kleeman, M. J., J. J. Schauer, and G. R. Cass, Size and composition distribution of fine particulate matter emitted from motor vehicles, *Environ. Sci. Technol.*, *34*, 1132–1142, 2000.

Kogan, Z. N., Y. L. Kogan, and D. K. Lilly, Evaluation of sulfate aerosols indirect effect in marine stratocumulus clouds using observation-derived cloud climatology, *Geophys. Res. Lett.*, *23*, 1937–1940, 1996.

Krishnamurti, T. N., B. Jha, J. Prospero, A. Jayaraman, and V. Ramanathan, Aerosol and pollutant transport and their impact on radiative forcing over the tropical Indian Ocean during the January–February 1996 pre-INDOEX cruise, *Tellus*, *Ser. B*, *50*, 521–542, 1998.

Langner, J., and H. Rodhe, A global three-dimensional model of the tropospheric sulfur cycle, *J. Atmos. Chem.*, *13*, 225–263, 1991.

Lavanchy, V. M. H., H. W. Gaggeler, U. Schotterer, M. Schwikowski, and U. Baltensperger, Historical record of carbonaceous particle concentrations from a European high-alpine glacier (Colle Gnifetti, Switzerland), *J. Geophys. Res.*, *104*, 21,227–21,236, 1999.

Lelieveld, J., et al., The Indian Ocean Experiment: Widespread air pollution from South and Southeast Asia, *Science*, *291*, 1031–1036, 2001.

Leon, J. F., et al., Large-scale advection of continental aerosols during INDOEX, *J. Geophys. Res.*, this issue.

Le Treut, H., M. Forichon, O. Boucher, and Z. X. Li, Sulfate aerosol indirect effect and CO_2 greenhouse forcing: Equilibrium response of the LMD GCM and associated cloud feedbacks, *J. Clim.*, *11*, 1673–1684, 1998.

Levitus, S., J. I. Antonov, T. P. Boyer, and C. Stephens, Warming of the world ocean, *Science*, *287*, 2225–2229, 2000.

Liao, H., and J. H. Seinfeld, Effect of clouds on direct aerosol radiative forcing of climate, *J. Geophys. Res.*, *103*, 3781–3788, 1998.

Lubin, D., J.-P. Chen, P. Pilewskie, V. Ramanathan, and F. P. J. Valero, Microphysical examination of excess cloud absorption in the tropical atmosphere, *J. Geophys. Res.*, *101*, 16,961–16,972, 1996.

Martin, G. M., D. W. Johnson, and A. Spice, The measurement and parameterization of effective radius of droplets in warm stratocumulus clouds, *J. Atmos. Sci.*, *51*, 1823–1842, 1994.

McFarquhar, G. M., and A. J. Heymsfield, Parameterizations of INDOEX microphysical measurements and calculations of cloud susceptibility: Applications for climate studies, *J. Geophys. Res.*, this issue.

McMurry, P. H., X. Zhang, and C.-T. Lee, Issues in aerosol measurement for optics assessments, *J. Geophys. Res.*, *101*, 19,189–19,197, 1996.

Meehl, G. A., W. M. Washington, D. J. Erickson III, B. P. Briegleb, and P. J. Jaumann, Climate change from increased CO_2 and direct and indirect effects of sulfate aerosols, *Geophys. Res. Lett.*, *23*, 3755–3758, 1996.

Meywerk, J., and V. Ramanathan, Observations of the spectral clear-sky aerosol forcing over the tropical Indian Ocean, *J. Geophys. Res.*, *104*, 24,359–24,370, 1999.

Nemesure, S., R. Wagener, and S. E. Schuartz, Direct shortwave forcing of climate by the anthropogenic sulfate aerosol: Sensitivity to particle size, composition, and relative humidity, *J. Geophys. Res.*, *100*, 26,105–26,116, 1995.

Nigam, S., C. Chung, and E. DeWeaver, ENSO diabatic heating in ECMWF and NCEP-NCAR reanalyses, and NCAR CCM3 simulation, *J. Clim.*, *13*, 3152–3171, 2000.

Novakov, T., D. A. Hegg, and P. V. Hobbs, Airborne measurements of carbonaceous aerosols on the East Coast of the United States, *J. Geophys. Res.*, *102*, 30,023–30,030, 1997.

Novakov, T., M. O. Andreae, R. Gabriel, T. W. Kirchstetter, O. L. Mayol-Bracero, and V. Ramanathan, Origin of carbonaceous aerosols over the tropical Indian Ocean: Biomass burning or fossil fuels?, *Geophys. Res. Lett.*, *27*, 4061–4064, 2000.

Oberhuber, J. M., An atlas based on the 'COADS' data set: The budgets of heat, buoyancy and turbulent kinetic energy at the surface of the global ocean, *Tech. Rep. 15*, Max-Planck Inst. for Meteorol., Hamburg, Germany, 1988.

Ogren, J. A., et al., Measurements of the size dependence of the concentration of non-volatile material in fog droplets, *Tellus*, *Ser. B*, *44*, 570–580, 1992.

Penner, J. E., R. E. Dickinson, and C. A. O'Neill, Effects of aerosol from biomass burning on the global radiation budget, *Science*, *256*, 1432–1434, 1992.

Pilinis, C., S. N. Pandis, and J. H. Seinfeld, Sensitivity of direct climate forcing by atmospheric aerosols to aerosol size and composition, *J. Geophys. Res.*, *100*, 18,739–18,754, 1995.

Podgorny, I. A., W. C. Conant, V. Ramanathan, and S. K. Satheesh, Aerosol modulation of atmospheric and surface solar heating rates over the tropical Indian Ocean, *Tellus*, *Ser. B*, *52*, 947–958, 2000.

Posfai, M., J. R. Anderson, P. R. Buseck, and H. Sievering, Soot and sulfate aerosol particles in the remote marine troposphere, *J. Geophys. Res.*, *104*, 21,685–21,693, 1999.

Raes, F., T. Bates, F. McGovern, and M. VanLiedekerke, The 2nd Aerosol Characterization Experiment (ACE-2): General overview and main results, *Tellus*, *Ser. B*, *52*, 111–125, 2000.

Rajeev, K., and V. Ramanathan, Direct observations of clear-sky aerosol radiative forcing from space during the Indian Ocean Experiment, *J. Geophys. Res.*, in press, 2001.

Rajeev, K., V. Ramanathan, and J. Meywerk, Regional aerosol distribution and its long-range transport over the Indian Ocean, *J. Geophys. Res.*, *105*, 2029–2043, 2000.

Ramanathan, V., et al., Indian Ocean Experiment (INDOEX) white paper, Scripps Inst. of Oceanogr., La Jolla, Calif., 1995.

Ramanathan, V., et al., Indian Ocean Experiment (INDOEX), A multi-agency proposal for field experiment in the Indian Ocean, 83 pp., *Publ. 162*, Scripps Inst. of Oceanogr., La Jolla, Calif., 1996.

Rasmusson, E. M., and T. H. Carpenter, The relationship between eastern equatorial Pacific sea surface temperatures and rainfall over India and Sri Lanka, *Mon. Weather Rev.*, *111*, 517–528, 1983.

Rosenfeld, D., Suppression of rain and snow by urban and industrial air pollution, *Science*, *287*, 1793–1796, 2000.

Russell, P. B., J. M. Livingston, P. Hignett, S. Kinne, J. Wong, A. Chien, R. Bergstrom, P. Durkee, and P. V. Hobbs, Aerosol-induced radiative flux changes off the United States mid-Atlantic coast: Comparison of values calculated from sunphotometer and in situ data with those measured by airborne pyranometer, *J. Geophys. Res.*, *104*, 2289–2307, 1999.

Satheesh, S. K., and V. Ramanathan, Large differences in the tropical aerosol forcing at the top of the atmosphere and Earth's surface, *Nature*, *405*, 60–63, 2000.

Satheesh, S. K., V. Ramanathan, X. Li-Jones, J. M. Lobert, I. A. Podgorny, J. M. Prospero, B. N. Holben, and N. G. Loeb, A model for the natural and anthropogenic aerosols over the tropical Indian Ocean derived from Indian Ocean Experiment data, *J. Geophys. Res.*, *104*, 27,421–27,440, 1999.

Schwartz, S. E., The whitehouse effect—Shortwave radiative forcing of climate by anthropogenic aerosols—An overview, *J. Aerosol Sci.*, *27*, 359–382, 1996.

Snider, J. R., and J. L. Brenguier, Cloud condensation nuclei and cloud droplet measurements during ACE-2, *Tellus*, *Ser. B*, *52*, 828–842, 2000.

Tahnk, W. R., INDOEX aerosol optical depths and radiative forcing derived from AVHRR, Ph.D. dissertation, 158 pp., Oreg. State Univ., Feb. 2001.

Taylor, J. P., and A. McHaffie, Measurements of cloud susceptibility, *J. Atmos. Sci.*, *51*, 1298–1306, 1994.

Twomey, S., *Atmospheric Aerosols*, 302 pp., Elsevier Sci., New York, 1977.

Valero, F. P., A. Bucholtz, B. C. Bush, and S. K. Pope, Climate forcing by anthropogenic aerosols over the Indian Ocean during INDOEX (abstract), *Eos Trans. AGU*, *80*(46), Fall Meet. Suppl., 162, 1999.

Weilicki, B. A., B. R. Barkstrom, E. F. Harrison, R. B. Lee III, G. L. Smith, and J. E. Cooper, Clouds and the Earth Radiant Energy System (CERES): An Earth observing system experiment, *Bull. Am. Meteorol. Soc.*, *77*, 853–868, 1996.

D. Althausen and J. Heintzenberg, Institute for Tropospheric Research, Leipzig D-04318, Germany.

J. Anderson, Department of Geology and Chemistry, Arizona State University, Tempe, AR 85287.

M. O. Andreae and J. Lelieveld, Max Planck Institute for Chemistry, Mainz 55020, Germany.

W. Cantrell, Department of Chemistry, Indiana University, Bloomington, IN 47401.

G. R. Cass, School of Civil and Environmental Engineering, Georgia Institute of Technology, Atlanta, GA 30332.

C. E. Chung, W. C. Conant, P. J. Crutzen, D. Lubin, I. A. Podgorny, V. Ramanathan (corresponding author), S. Rupert, S. K. Satheesh, and F. P. J. Valero, Center for Atmospheric Sciences, Scripps Institution of Oceanography, University of California, San Diego, CA 92037. (ram@fiji.ucsd.edu)

A. D. Clarke and S. Howell, Department of Oceanography, University of Hawaii, Honolulu, HI 96822.

J. A. Coakley, College of Oceanic and Atmospheric Sciences, Oregon State University, Corvallis, OR 97331.

W. D. Collins, A. J. Heymsfield, J. T. Kiehl, G. McFarquhar, and P. Rasch, National Center for Atmospheric Research, Boulder, CO 80307.

F. Dulac, Laboratoire des Sciences du Climat et de l'Environment, Gif sur Yvette 91191, France.

B. Holben, NASA Goddard Space Flight Center, Greenbelt, MD 20771.

J. Hudson, Desert Research Institute, Reno, NV 89506.

A. Jayaraman, Physical Research Laboratory, Ahmedabad 380-009, India.

T. N. Krishnamurti, Department of Meteorology, Florida State University, Tallahassee, FL 32306.

A. P. Mitra, National Physical Laboratory, New Delhi 110 012, India.

T. Novakov, Lawrence Berkeley National Laboratory, Berkeley, CA 94720.

J. A. Ogren and P. Sheridan, Climate Monitoring and Diagnostics Laboratory, NOAA, Boulder, CO 80303.

K. Prather, Department of Chemistry, University of California, Riverside, CA 92521.

K. Priestley, NASA Langley Research Center, Hampton, VA 23665.

J. M. Prospero, Rosenstiel School of Marine and Atmospheric Science, University of Miami, Miami, FL 33149.

P. K. Quinn, Pacific Marine Environmental Laboratory, NOAA, Seattle, WA 98115.

K. Rajeev, Space Physics Laboratory, VSSC, Thiruvananthapuram 695022, Kerala State, India.

R. Sadourny, Laboratoire de Meteorologie Dynamique, Paris 75005, France.

G. E. Shaw, Geophysical Institute, University of Alaska Fairbanks, Fairbanks, AK 99775.

(Received October 3, 2000; revised February 27, 2001;
accepted February 27, 2001.)